Tropical Pacific and Atlantic Climate Variability in CCSM3

CLARA DESER

National Center for Atmospheric Research, Boulder, Colorado

ANTONIETTA CAPOTONDI

NOAA–CIRES Climate Diagnostics Center, Boulder, Colorado

R. SARAVANAN AND ADAM S. PHILLIPS

National Center for Atmospheric Research, Boulder, Colorado

(Manuscript received 26 January 2005, in final form 4 August 2005)

ABSTRACT

Simulations of the El Niño–Southern Oscillation (ENSO) phenomenon and tropical Atlantic climate variability in the newest version of the Community Climate System Model [version 3 (CCSM3)] are examined in comparison with observations and previous versions of the model. The analyses are based upon multicentury control integrations of CCSM3 at two different horizontal resolutions (T42 and T85) under present-day CO_2 concentrations. Complementary uncoupled integrations with the atmosphere and ocean component models forced by observed time-varying boundary conditions allow an assessment of the impact of air–sea coupling upon the simulated characteristics of ENSO and tropical Atlantic variability.

The amplitude and zonal extent of equatorial Pacific sea surface temperature variability associated with ENSO is well simulated in CCSM3 at both resolutions and represents an improvement relative to previous versions of the model. However, the period of ENSO remains too short (2–2.5 yr in CCSM3 compared to 2.5–8 yr in observations), and the sea surface temperature, wind stress, precipitation, and thermocline depth responses are too narrowly confined about the equator. The latter shortcoming is partially overcome in the atmosphere-only and ocean-only simulations, indicating that coupling between the two model components is a contributing cause. The relationships among sea surface temperature, thermocline depth, and zonal wind stress anomalies are consistent with the delayed/recharge oscillator paradigms for ENSO. We speculate that the overly narrow meridional scale of CCSM3's ENSO simulation may contribute to its excessively high frequency. The amplitude and spatial pattern of the extratropical atmospheric circulation response to ENSO is generally well simulated in the T85 version of CCSM3, with realistic impacts upon surface air temperature and precipitation; the simulation is not as good at T42.

CCSM3's simulation of interannual climate variability in the tropical Atlantic sector, including variability intrinsic to the basin and that associated with the remote influence of ENSO, exhibits similarities and differences with observations. Specifically, the observed counterpart of El Niño in the equatorial Atlantic is absent from the coupled model at both horizontal resolutions (as it was in earlier versions of the coupled model), but there are realistic (although weaker than observed) SST anomalies in the northern and southern tropical Atlantic that affect the position of the local intertropical convergence zone, and the remote influence of ENSO is similar in strength to observations, although the spatial pattern is somewhat different.

1. Introduction

The El Niño–Southern Oscillation (ENSO) phenomenon is arguably the most important deterministic source of interannual climate variability worldwide (Pan and Oort 1983; Ropelewski and Halpert 1987; Kiladis and Diaz 1989; Philander 1990; Glantz 2000; among others). Due primarily to coupled ocean–atmosphere interaction within the tropical Pacific, ENSO is manifest as irregular warmings and coolings of the surface waters of the eastern equatorial Pacific lasting typically 1–1.5 yr and recurring approximately every 3–8 yr, accompanied by changes in atmospheric circu-

Corresponding author address: Dr. Clara Deser, Climate and Global Dynamics Division, National Center for Atmospheric Research, P.O. Box 3000, Boulder, CO 80307-3000.
E-mail: cdeser@ucar.edu

lation, rainfall, and upper-ocean heat content (Rasmusson and Carpenter 1982; Deser and Wallace 1990; Harrison and Larkin 1998; Meinen and McPhaden 2000; Trenberth et al. 2002; among others). The tropical precipitation anomalies force remote atmospheric circulation changes that in turn alter the climate in many parts of world (Horel and Wallace 1981; Trenberth et al. 1998; Alexander et al. 2002; among others). Coupled air–sea interactions in the tropical Atlantic sector also have important consequences for climate over the adjacent continents and Europe (see Xie and Carton 2004 for a recent review).

Global coupled ocean–atmosphere general circulation models simulate ENSO with varying degrees of realism (Latif et al. 2001; McAvaney et al. 2001; Davey et al. 2002; AchutaRao and Sperber 2002). In general, the models' ENSO variability tends to be more regular and at a higher frequency (2–3-yr periodicity) than nature's, and the simulated tropical Pacific SST variability tends to extend too far to the west and is more narrowly confined about the equator than observed. [A recent exception is the high-resolution (T106 atmospheric component) coupled model integration reported by Guilyardi et al. (2004).] A number of potential causes for these model deficiencies have been identified, including insufficient high-frequency stochastic atmospheric variability, which enhances the regularity of ENSO (Kleeman and Moore 1997; Blanke et al. 1997); reduced meridional extent and amplitude of the zonal wind stress anomalies in the western and central equatorial Pacific, which increases the frequency of ENSO (Kirtman 1997; Jin 1997b; Guilyardi et al. 2003, 2004); and a westward-extended mean equatorial cold tongue, which would increase SST variability in the western half of the basin (Kiehl and Gent 2004). The models' ENSO variability is generally consistent with the "delayed oscillator" mechanism (Schopf and Suarez 1988; Battisti and Hirst 1989; Kirtman 1997; Jin 1997a; Fedorov and Philander 2000), the leading dynamical paradigm for ENSO (Latif et al. 2001; Otto-Bliesner and Brady 2001; Davey et al. 2002). Recently, a "recharge oscillator" paradigm has been proposed (Jin 1997a,b) that is dynamically consistent with the delayed oscillator but emphasizes meridional mass transports rather than wave processes. Some observational studies (Meinen and McPhaden 2000; Kessler 2002) have shown that the interannual evolution of equatorial Pacific heat content anomalies is consistent with the recharge oscillator mechanism, but analogous diagnostics have not been commonly applied to coupled general circulation model simulations of ENSO.

Atmospheric circulation changes forced by ENSO-related tropical precipitation anomalies initiate climate impacts worldwide. One of the most robust extratropical atmospheric circulation teleconnections associated with ENSO is a deepening and eastward extension of the wintertime Aleutian low pressure cell over the North Pacific during warm events compared to cold events (Horel and Wallace 1981; Trenberth 1991; Trenberth et al. 1998; Hoerling and Kumar 2002; Alexander et al. 2002; among others). This anomalous circulation brings enhanced precipitation to the southwestern United States and warmer air temperatures to northwestern North America (Ropelewski and Halpert 1987; Kiladis and Diaz 1989; Minobe 1997). An analogous atmospheric teleconnection forced by ENSO occurs over the South Pacific and South America during austral winter (cf., Kiladis and Mo 1998). The ability of general circulation models to correctly represent the extratropical atmospheric circulation response to ENSO depends on a variety of factors, including the spatial distribution of the tropical rainfall anomalies, the strength and location of the midlatitude stationary waves and storm tracks, and the barotropic instability of the background flow (DeWeaver and Nigam 2004 and references therein).

Climate variability in the tropical Atlantic sector includes that intrinsic to the basin and that associated with the remote influence of ENSO (Xie and Carton 2004). The former has been characterized in terms of two spatial patterns: a cross-equatorial SST anomaly gradient that affects the position of the Atlantic intertropical convergence zone (ITCZ), and an equatorial SST anomaly analogous to ENSO in the Pacific. Thermodynamic air–sea interaction is believed to be responsible for the cross-equatorial gradient pattern while dynamical air–sea interaction is important for the equatorial mode. The remote influence of ENSO is initiated by surface heat flux anomalies associated with atmospheric teleconnections from the tropical Pacific. These aspects of tropical Atlantic variability (TAV) are generally not well simulated in coupled general circulation models (Xie and Carton 2004).

In this study, we document aspects of ENSO and TAV in the newest version of the Community Climate System Model [version 3 (CCSM3)], a state-of-the-art coupled general circulation model, in comparison with observations and previous versions of CCSM. CCSM3 contains significant improvements over previous releases, including a diurnal cycle of penetrating solar radiation in the upper ocean that results in a more realistic mean SST distribution across the tropical Pacific (Large and Danabasoglu 2006), an aspect particularly relevant for this study. Our analyses are based upon extended (multicentury) control integrations under present-day CO_2 values at two different horizontal

resolutions (T42 and T85 for the atmospheric and terrestrial components, coupled to 1° ocean and sea ice components), allowing us to examine the impact of resolution upon the simulated characteristics of ENSO and TAV. We also compare CCSM3 with uncoupled integrations of both the atmosphere and ocean component models forced by observed time-varying boundary conditions, enabling us to assess the influence of air–sea coupling upon the simulated behavior of ENSO and TAV.

The paper is structured as follows. Section 2 contains brief descriptions of CCSM3 and the uncoupled atmosphere and ocean model integrations, as well as the observational datasets and analysis procedures used in this study. Section 3a documents the spatial and temporal characteristics of the simulated ENSO phenomenon in the Tropics in both versions (T42 and T85) of CCSM3, including the patterns of SST, thermocline depth, precipitation, surface air temperature, and sea level pressure (SLP) anomalies. Section 3b documents the global response patterns of SLP and 500-hPa geopotential height anomalies to ENSO at both model resolutions, as well as those from a five-member ensemble of uncoupled integrations with the atmospheric model component forced by observed time-varying global SSTs during 1950–2000. Section 3c presents a more mechanistic analysis of ENSO thermocline depth variability in the context of the delayed oscillator mechanism. The results of this analysis suggest that the strength and meridional scale of the surface wind response to ENSO SST anomalies may impact the frequency of ENSO in the model. The nature of the surface wind response and implications for air–sea energy exchange are explored further in section 3d. Section 4 documents aspects of interannual climate variability in the tropical Atlantic sector, including variability intrinsic to the basin and that associated with the remote influence of ENSO.

2. Model description, observational datasets, and analysis procedures

CCSM3 is a state-of-the art coupled general circulation model comprised of four components (atmosphere, ocean, land, and cryosphere) linked by means of a flux coupler. The atmospheric component, the Community Atmosphere Model version 3 (CAM3), is a global general circulation model with 26 vertical levels and an Eulerian spectral dynamical core with triangular truncation at T42 or T85 (a T31 version is also available), corresponding to a horizontal resolution of 2.8° or 1.4°, respectively. The ocean component is based upon the Parallel Ocean Program (POP) model version 1.4.3 from the Los Alamos National Laboratory. POP has 40 vertical levels, a horizontal resolution of 1°, and a dipolar grid. The land surface model grid is identical to that of CAM3, and the sea ice model grid is the same as POP's.

CCSM3 contains significant revisions over previous releases, including new treatments of cloud processes, aerosol radiative forcing, sea ice dynamics, and a diurnal cycle of penetrating solar radiation in the upper ocean. Further details on model changes and configuration are provided in Collins et al. (2006). The CCSM3 simulations analyzed in this study are the extended (>600 yr) coupled control integrations at T42 and T85 resolution under 1990 CO_2 concentrations; note that CCSM3 does not utilize flux corrections. Unless stated otherwise, the ENSO and TAV analyses presented in this paper are based upon model years 100–799 for CCSM3 (T42), 100–599 for CCSM3 (T85), and 350–999 for CCSM2 (T42); the mean SST field over the tropical Atlantic from CSM1, presented briefly in section 4, is based upon model years 1–100. The analyses of CCSM3 begin in year 100 to minimize any potential climate drifts that may have occurred at the beginning of the simulations; those for CCSM2 begin in year 350 because of a change in model parameters in that year (see Kiehl and Gent 2004). The ending dates for the model analyses reflect the latest year of simulation available to us at the time this study was undertaken. The reader is referred to Boville and Gent (1998) and Kiehl and Gent (2004) for descriptions of CSM1 and CCSM2, respectively.

In addition to CCSM3, this study makes use of two five-member ensemble CAM3 integrations (one at T42 and one at T85) forced by observed global time-varying SSTs and sea ice concentrations during 1950–2000 taken from J. W. Hurrell et al. (2004, personal communication). Different initial conditions are used for each member of the CAM3 Atmospheric Model Intercomparison Project (AMIP)-style integrations. We also analyze thermocline variability in an uncoupled integration of the 1° POP ocean model forced by observed global time-varying surface atmospheric conditions based on National Centers for Environmental Research–National Center for Atmospheric Research (NCEP–NCAR) reanalyses (Kalnay et al. 1996) during 1958–2000. The details of the forcing fields for this simulation, which include surface air temperature and humidity, wind speed, and radiation, may be found in Large and Danabasoglu (2006).

The following obervational datasets are used: 1) SLP, surface wind and wind stress, turbulent latent and sensible heat fluxes at the sea surface, and 500-hPa geopotential heights from the NCEP–NCAR reanalyses (Kalnay et al. 1996) during 1950–2001 on a 2.5° grid (T62

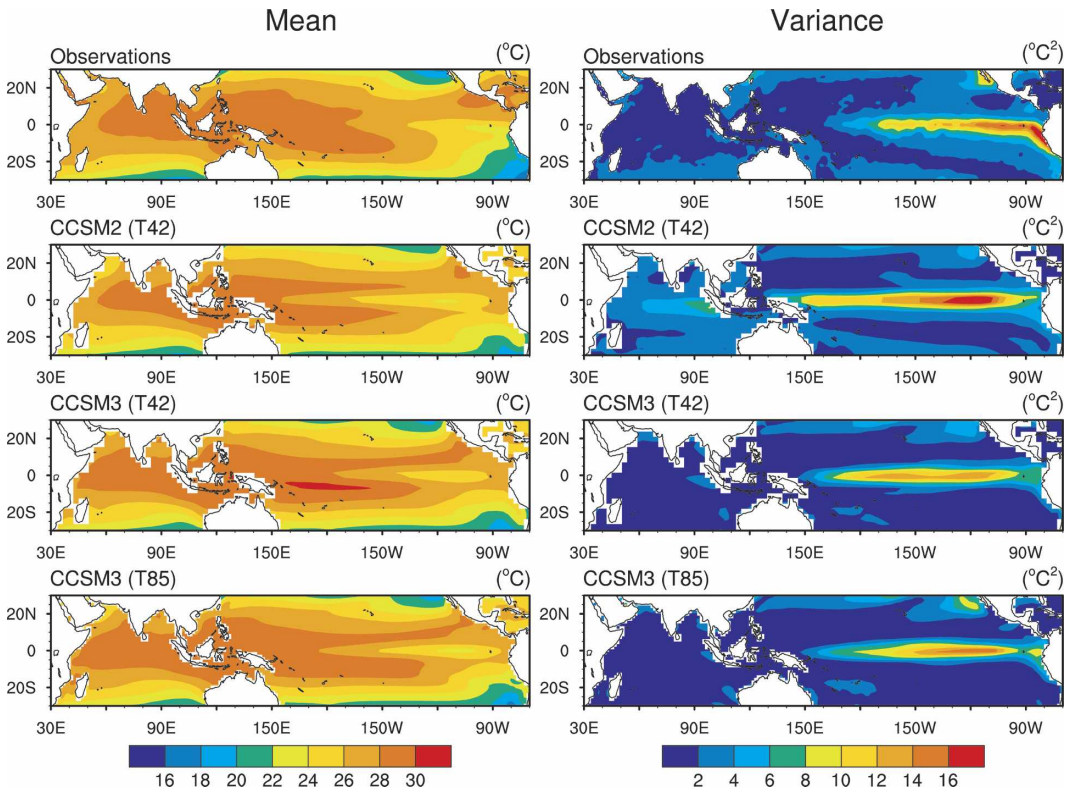

FIG. 1. SST long-term annual (left) means and (right) variances from observations, CCSM2 (T42), CCSM3 (T42), and CCSM3 (T85). Variances are computed from monthly anomalies (departures from the long-term monthly means). Color scales are given at the bottom of each column of maps.

Gaussian grid for heat fluxes); 2) SST from the Hadley Centre Sea Ice and SST (HadISST) dataset (Rayner et al. 2003) during 1900–2003 on a 1° grid; 3) air temperature over land from the Climatic Research Unit (CRU) Surface Temperature (TS) 2.0 dataset (Mitchell et al. 2003, manuscript submitted to *J. Climate*); 4) precipitation from Xie and Arkin (1997) based on blended satellite and in situ measurements during 1979–2001 on a 2.5° grid; 5) SST, SLP, and surface winds from the International Comprehensive Ocean–Atmosphere Data Set (ICOADS; Woodruff et al. 1987) during 1950–97 on a 2° grid; and 6) surface shortwave and longwave radiation from the International Satellite Cloud Climatology Project (ISCCP; Zhang et al. 2004) during 1984–2000 on a 2.5° grid.

The simple analysis methods used in this study include compositing, linear regression and correlation analysis, and empirical orthogonal function (EOF) analysis. Statistical significance of the composite and regression fields is assessed by means of a local Student's *t* test. Monthly anomalies are defined by subtracting the long-term monthly means from the individual monthly values for a given year.

3. ENSO

a. *Tropical Indo-Pacific SST and thermocline depth variability*

The long-term annual mean distributions of SST and the variances of monthly anomalies of SST in the tropical Indo-Pacific for observations (HadISST, years 1950–2000), CCSM2 (T42), and CCSM3 (T42 and T85) are compared in Fig. 1. The simulation of the long-term mean SST distribution is improved in CCSM3 relative to CCSM2: in particular, the equatorial "cold tongue" is less pronounced and does not extend as far west, although it is still somewhat stronger than observed. The improvement of the cold tongue bias in CCSM3 is primarily due to the inclusion of a diurnal cycle in penetrating solar radiation in the ocean model component (see Large and Danabasoglu 2006). The largest SST anomaly variance occurs in the equatorial cold tongue; however, differences in spatial extent and amplitude are apparent and likely associated with biases in the mean state. For example, the exaggerated strength of the cold tongue in CCSM2 (Kiehl and Gent 2004) produces variability that is too large and extends too far

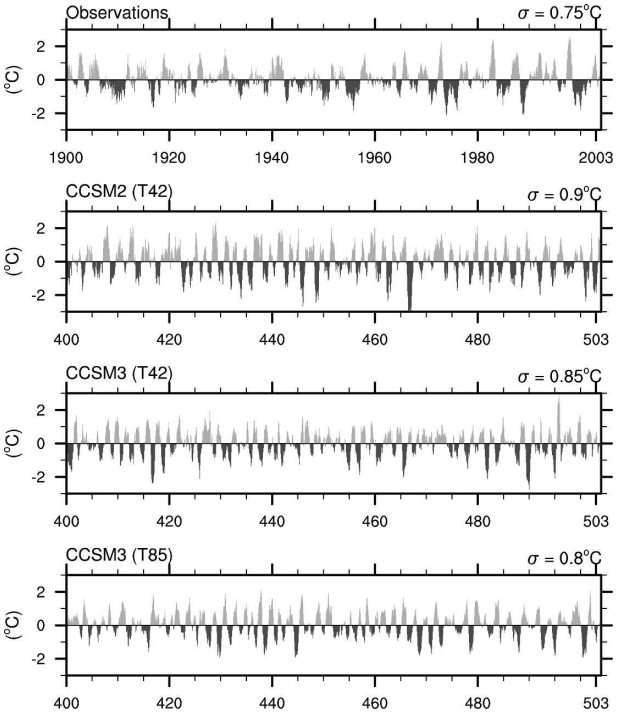

FIG. 2. Time series of monthly SST anomalies (°C) in the Niño-3.4 region from observations (HadISST, 1900–2003), CCSM2 (T42), CCSM3 (T42), and CCSM3 (T85). A 104-yr segment is shown for each model simulation (model years 400–503) to match the record length available for observations. The standard deviations of the time series are given at the upper right of each panel (note that these are based upon the full set of model years analyzed).

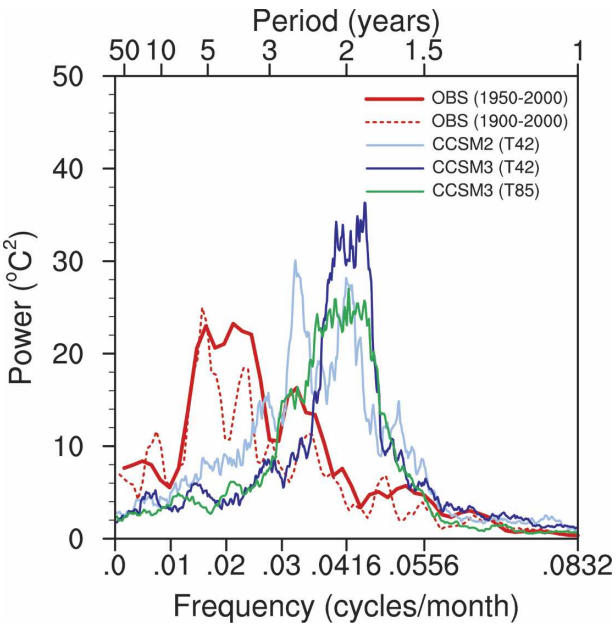

FIG. 3. Power spectra of the monthly Niño-3.4 SST anomaly time series from observations (HadISST, years 1900–2000 and 1950–2000), CCSM2 (T42, model years 350–999), CCSM3 (T42, model years 100–799), and CCSM3 (T85, model years 100–599).

west. The T85 version of CCSM3 exhibits the most realistic representation of the variability, with maximum values (16°C^2) east of 130°W and a secondary maximum along the South American coast (although the latter is underestimated).

A commonly used index for representing SST variability associated with ENSO is the area average of monthly SST anomalies in the region 5°N–5°S, 170°–120°W, referred to as the "Nino-3.4 SST index" (see, e.g., Trenberth et al. 2002). This region is located within the area of maximum SST variance and also lies within the center of action of the leading EOF pattern of monthly SST anomalies (not shown): the associated principal component (PC) time series exhibits a correlation coefficient with the Niño-3.4 SST index in excess of 0.95 for each model and for observations. The Niño-3.4 SST indices from observations and the models are shown in Fig. 2: 104-yr samples from each model integration are shown to facilitate comparison with the period of record available from observations (1900–2003). A visual comparison of the Niño-3.4 SST records reveals that, in all cases, the simulated variability is too rapid and regular compared to observations. It can also be seen that the amplitude of the Niño-3.4 variability is overestimated in CCSM2 (standard deviation = 0.9 K for model years 350–999) compared to observations (standard deviation = 0.75 K), but more realistic in CCSM3 (standard deviation = 0.85 K for T42 based upon model years 350–999 and 0.80 K for T85 based upon model years 100–599), consistent with the results shown in Fig. 1. The amplitude of the variability in CSM1 is more than a factor of 2 smaller than in CCSM2 [not shown, but see Kiehl and Gent (2004)].

The frequency and amplitude of ENSO is quantified by performing a power spectrum analysis on the Niño-3.4 time series (Fig. 3). The observational results are shown for two periods, 1900–2003 and 1950–2003, to give an indication of the sensitivity of the results to different record lengths. Consistent with one's visual impression of the Niño-3.4 time series, the dominant frequencies in the model power spectra (~1.8–3 yr) are too high relative to observations (~3–8 yr; there is some overlap between observations and the models around 2.5 yr, but this is not the dominant frequency in either nature or CCSM3). The effect of increased model resolution in CCSM3 is to slightly broaden the spectral peak toward lower frequencies, but it is very minor and does not extend to periods longer than 3 yr. (Note that CCSM2 at T42 resolution also exhibits enhanced variance around 2.5 yr, suggesting that model

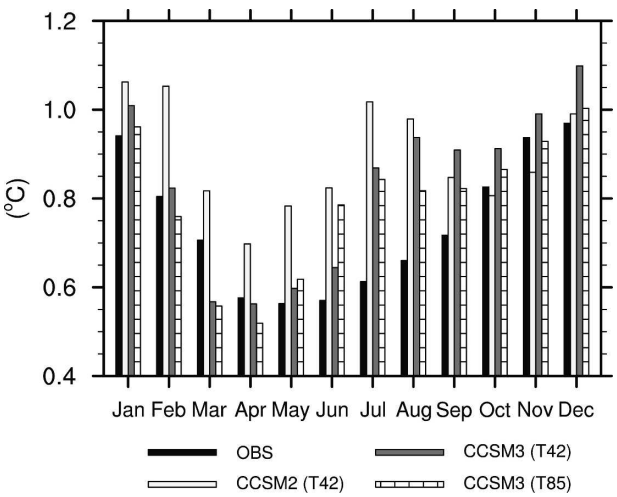

FIG. 4. Monthly standard deviations (°C) of the Niño-3.4 SST anomaly time series from observations (HadISST, years 1900–2003), CCSM2 (T42), CCSM3 (T42), and CCSM3 (T85).

resolution is not the only cause for enhancing the low-frequency end of the dominant spectral peak.) Finally, an examination of the power spectra for individual 100-yr segments of the Niño-3.4 index from CCSM3 at T85 resolution reveals no significant departures from the dominant frequencies seen in the full 700 yr of record (not shown).

The seasonal cycle of the standard deviation of the Niño-3.4 SST anomaly time series from observations and the models is shown in Fig. 4. The observed Niño-3.4 record exhibits minimum variability during April–June and maximum variance near the end of the calendar year (November–January). Both CCSM3 records show a seasonal cycle similar to observations except in boreal summer when they overestimate the variance by approximately a factor of 2. Overall, CCSM3 yields a more realistic amplitude and seasonal cycle of Niño-3.4 variability than CCSM2 (in CCSM2, the standard deviations during February–August are nearly twice as large as observed). It is interesting to note that CCSM3's reasonable simulation of the seasonal cycle of interannual variability occurs despite a poor simulation of the seasonal cycle of the mean SST (Large and Danabasoglu 2006).

As discussed in the introduction, equatorial ocean dynamics play a key role in the evolution of ENSO. The primary variable for equatorial ocean dynamical processes is thermocline depth, a quantity that reflects the amount of heat stored in the upper ocean. Figure 5a shows the seasonal evolution of simulated thermocline depth, as given by the depth of the 15°C isotherm, and observed SST anomalies during a composite ENSO cycle. The simulated thermocline depth values are obtained from the ocean model component of CCSM3 forced by observed surface fields during 1958–2000 (recall section 2). The 15°C isotherm, located in the core of the main thermocline, provides similar dynamical information as the 20°C isotherm, the usual choice for thermocline depth in observations, but is less subject to influence from surface processes in regions where the thermocline is close to the surface, for example, the eastern part of the equatorial Pacific. The seasonal anomaly composites were constructed by averaging years in which the Niño-3.4 SST index in September–November [SON (hereafter 3-month periods are denoted by the first letter of each respective month); when the index is near its peak; recall Fig. 4] exceeds one standard deviation and subtracting the average of the years in which it is less than −1 standard deviation. The composites begin in MAM of the composite year (denoted MAM^0) and go through JJA of the following year (denoted JJA^{+1}). In lieu of direct observational estimates of the depth of the 15°C isotherm, which are sparse and limited in duration, we make use of thermocline depth anomalies from an integration of the ocean component of CCSM3 at T85 resolution (the POP model), forced by observed surface fields during 1958–2000 derived from the NCEP–NCAR reanalyses (Kalnay et al. 1996; see also Large and Danabasoglu 2006). The results compare well with the available observational and assimilated datasets of thermocline depth anomalies during ENSO, shown, for example, by Trenberth et al. (2002) and Meinen and McPhaden (2000). The observed SST anomaly composites are based on the years 1958–2000 to be compatible with the period of record available for thermocline depth.

The observed ENSO composite SST evolution (Fig. 5a) exhibits an incipient warming along the equator and coast of South America during MAM^0 that subsequently grows in amplitude over the next several seasons, reaching its peak around SON^0 and DJF^0. The warm event diminishes during MAM^{+1} and begins to transition to a weak cold event in JJA^{+1}. Accompanying the warming is the simultaneous development of negative SST anomalies in the northwest and southwest tropical Pacific. The Indian Ocean exhibits a delayed warming relative to that in the Pacific, reaching peak strength around MAM^{+1} but lingering through JJA^{+1} and beyond (not shown). Similar results are shown in Harrison and Larkin (1998), Rasmusson and Carpenter (1982), Trenberth et al. (2002), and Klein et al. (1999), among others.

At the beginning of the incipient warm event in MAM^0, thermocline depth anomalies display a zonally symmetric signal, with deeper-than-average values along the equator and shallower-than-average values

around 10°–15°N and 15°–25°S. This zonally symmetric signal may reflect conditions at the end of the prior cold event when there is a net import of upper-ocean heat content into the equatorial zone (see also Trenberth et al. 2002). As the warm event develops, the pattern of thermocline depth anomalies becomes more zonally asymmetric, with deeper values in the east and shallower values in the west, reaching peak amplitude late in the calendar year. This configuration is consistent with a reduction in the slope of the thermocline driven by (and in balance with) a relaxation of the easterly winds along the equator (not shown). At the end of the warm event (JJA^{+1}), the thermocline depth anomalies begin to transition to a more zonally symmetric pattern of shallower values (depleted heat content) in the equatorial zone and deeper values (enhanced heat content) to the north and south, opposite to that at the beginning of the event. The temporal and spatial phase relationships between the composite ENSO SST and thermocline depth anomaly fields are qualitatively consistent with the delayed oscillator mechanism, as discussed previously by Trenberth et al. (2002) among others.

The ENSO composite evolutions of SST and thermocline depth anomalies from CCSM3 at T85 resolution are shown in Fig. 5b (results based upon the T42 model are similar; not shown). The development of positive SST anomalies along the equator from MAM^{0} through DJF^{+1} is similar to observations, but the transition to negative anomalies occurs one season ahead of nature (MAM^{+1} compared to JJA^{+1}) and the ensuing cold event is stronger than observed, consistent with the model's stronger biennial tendency. It is also apparent that the simulated SST warming is more narrowly confined about the equator compared to nature, and that the magnitude of the cooling in the western Pacific and the delayed warming in the Indian Ocean are substantially weaker than observed.

- The model's composite ENSO evolution of thermocline depth anomalies resembles observations in many respects. In particular, at the beginning of the warm event MAM^{0}, the thermocline is deeper than average throughout the equatorial Pacific, with weaker anomalies of opposite sign to the north and south. While the warm event develops over the next few seasons, the zonally symmetric pattern of thermocline depth anomalies transitions to a zonally asymmetric pattern, with maximum anomalous east–west gradient occurring in DJF^{+1} near the peak of the SST warming. At the end of the warm event and beginning of the ensuing cold event (MAM^{+1} and JJA^{+1}), the pattern of thermocline depth anomalies exhibits a strong zonally symmetric component indicative of a depletion of equatorial upper-ocean heat content; this pattern resembles that in MAM^{0} but with opposite phase, reflecting the overly biennial nature of the simulated ENSO cycle. The main discrepancy between the spatial patterns of simulated and observed thermocline depth anomalies is their meridional scale, which is considerably narrower in the model than in nature (cf., e.g., MAM^{0}, DJF^{+1}, or JJA^{+1}), similar to the results for SST. A more mechanistic analysis of the simulated thermocline depth anomalies within the framework of the delayed oscillator and recharge oscillator paradigms is given in section 3c.

b. *Global SST, precipitation, and atmospheric circulation anomaly composites*

In this section we describe selected aspects of the global ENSO anomaly patterns of surface temperature, precipitation, and atmospheric circulation in DJF and JJA. The Web supplement to this paper (http://www.cgd.ucar.edu/cas/cdeser/CCSM3ENSOsupfig.html) contains a complete set of figures showing warm-minus-cold ENSO anomaly composites of SST, surface air temperature, precipitation, SLP and 500-hPa geopotential heights for all four seasons from observations, CCSM3 at both resolutions, and the ensemble mean of the CAM3 AMIP integrations at both resolutions.

Warm-minus-cold ENSO composite difference maps of surface temperature (SST over oceans and air temperature over land) and precipitation during DJF are shown in Fig. 6 for observations, CCSM3 at T85 resolution (results for T42 look similar: see Web supplement), and the ensemble mean of the five CAM3 AMIP integrations at T85 resolution (results for T42 look similar: see Web supplement). Warm (cold) years were identified based on the criterion that the Niño-3.4 SST index exceeds one standard deviation (is less than –1 standard deviation). A simple Student's t test is used to assess the 99% a priori (95% a posteriori) significance levels for the composite differences at each grid point. The observed and CAM3 AMIP composites are based upon the period 1950–2000 (1979–2000 for precipitation because of the limited duration of the satellite record). The years used for the warm event composite are 1958, 1966, 1973, 1983, 1987, 1992, 1995, and 1998; and the years used for the cold event composite are 1950, 1956, 1971, 1974, 1976, 1985, 1989, 1999, and 2000.

Over the Tropics, the observed SST pattern consists of positive anomalies in the eastern Pacific, with maximum values (~4 K) along the equator spreading with

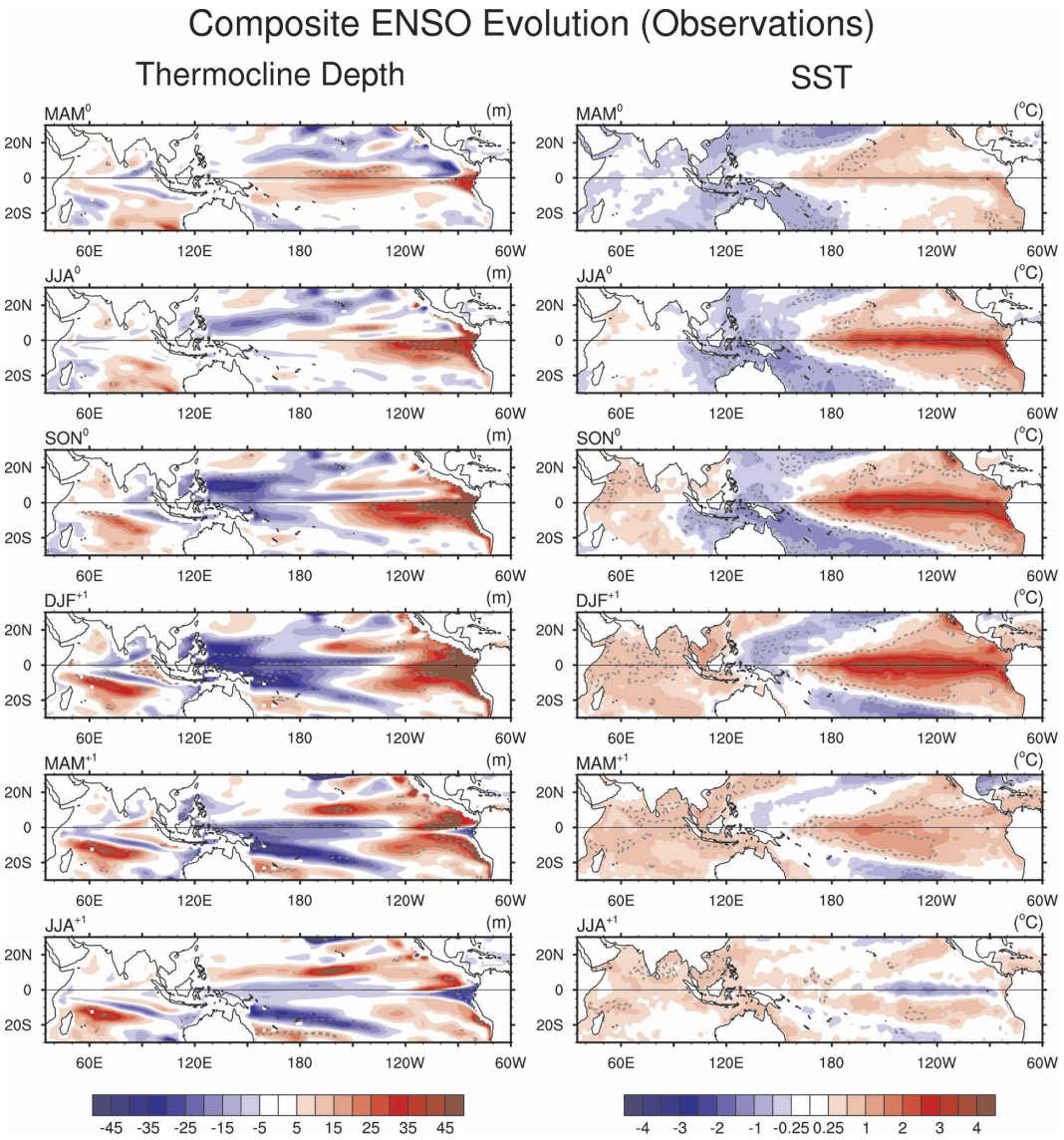

FIG. 5. (a) Seasonal evolution of (left) simulated thermocline depth and (right) observed SST anomalies during a composite warm ENSO event relative to a cold one (see text for details of the compositing procedure). The simulated thermocline depth values are obtained from the ocean model component of CCSM3 forced by observed surface fields during 1958–2000. Positive (negative) thermocline depth values indicate a deeper (shallower) thermocline relative to the long-term average. Dashed contours indicate that the anomalies are significantly different from zero at the 99% confidence level based upon a Student's *t* test.

reduced amplitude into the subtropics of both hemispheres in a wedge-shaped pattern; positive anomalies (~1 K) also occur in the tropical Indian Ocean. Negative SST anomalies are found along the flanks of the wedge-shaped area to the north and south and in the western equatorial Pacific, with amplitudes ~ -1 K. In the model, the tropical Pacific SST signal is largely confined to the equatorial zone where it extends westward to New Guinea. Unlike observations, there is almost no cooling on the flanks of this equatorially confined warming. Weaker positive anomalies are found over the tropical Indian Ocean, similar to observations.

In the extratropics, the model simulates the general features of the observed SST anomaly pattern: for example, in the Southern Hemisphere, the cooling to the southeast of Australia and warming in the Southern Ocean between 180° and 90°W; and in the Northern Hemisphere, the cooling in the central north Pacific and warming in the eastern north Pacific (albeit with considerably reduced amplitude). These extratropical

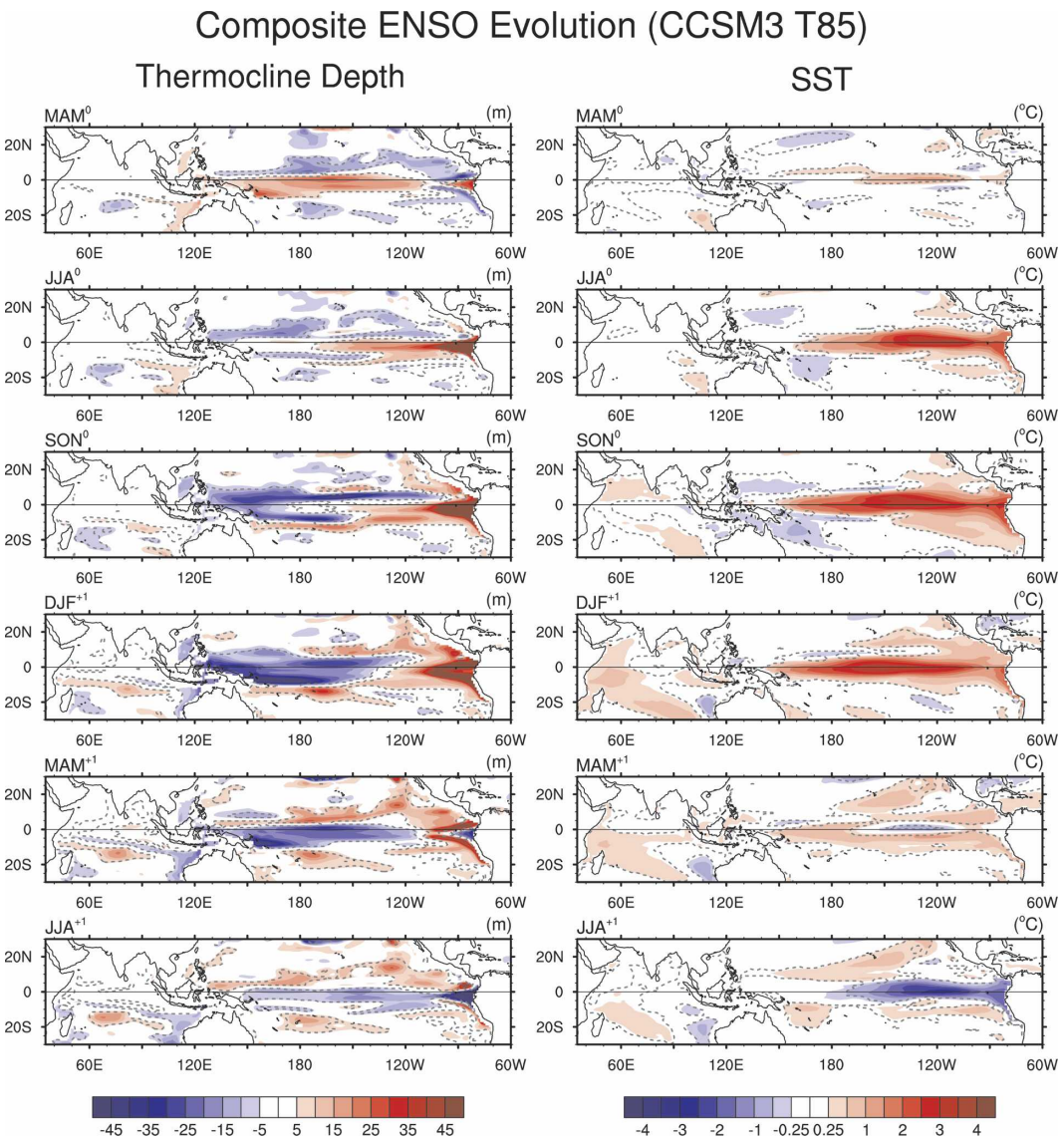

FIG. 5. (*Continued*) (b) Same as in (a), but for thermocline depth and SST from the CCSM3 simulation at T85 resolution based upon model years 100–599.

SST anomalies are likely driven by local atmospheric circulation changes associated with ENSO teleconnection patterns (see Fig. 9 and Alexander et al. 2006). Similarly, atmospheric circulation anomalies are responsible for positive surface air temperature anomalies over western North America, a feature that is well simulated in CCSM3. The model also exhibits realistic positive air temperature anomalies over Australia, western Africa and portions of southern Africa, and northern South America.

The distribution of tropical precipitation changes is closely associated with the pattern of SST anomalies in both observations and the model. In observations, enhanced precipitation is found over and near the region of positive SST anomalies in the eastern Pacific and western Indian Ocean; reduced precipitation occurs over Indonesia, the South Pacific convergence zone (SPCZ) in the southwest Pacific, and in the Atlantic ITCZ. CCSM3 also exhibits enhanced precipitation in the vicinity of the equatorial Pacific SST warming, but the compensating regions of reduced rainfall occur preferentially to the north and south rather than to the west over Indonesia as observed. Reduced rainfall is also found in the Atlantic ITCZ, similar to observations.

The precipitation anomalies associated with ENSO may also be viewed within the context of the climatological precipitation distribution (Fig. 7). In observa-

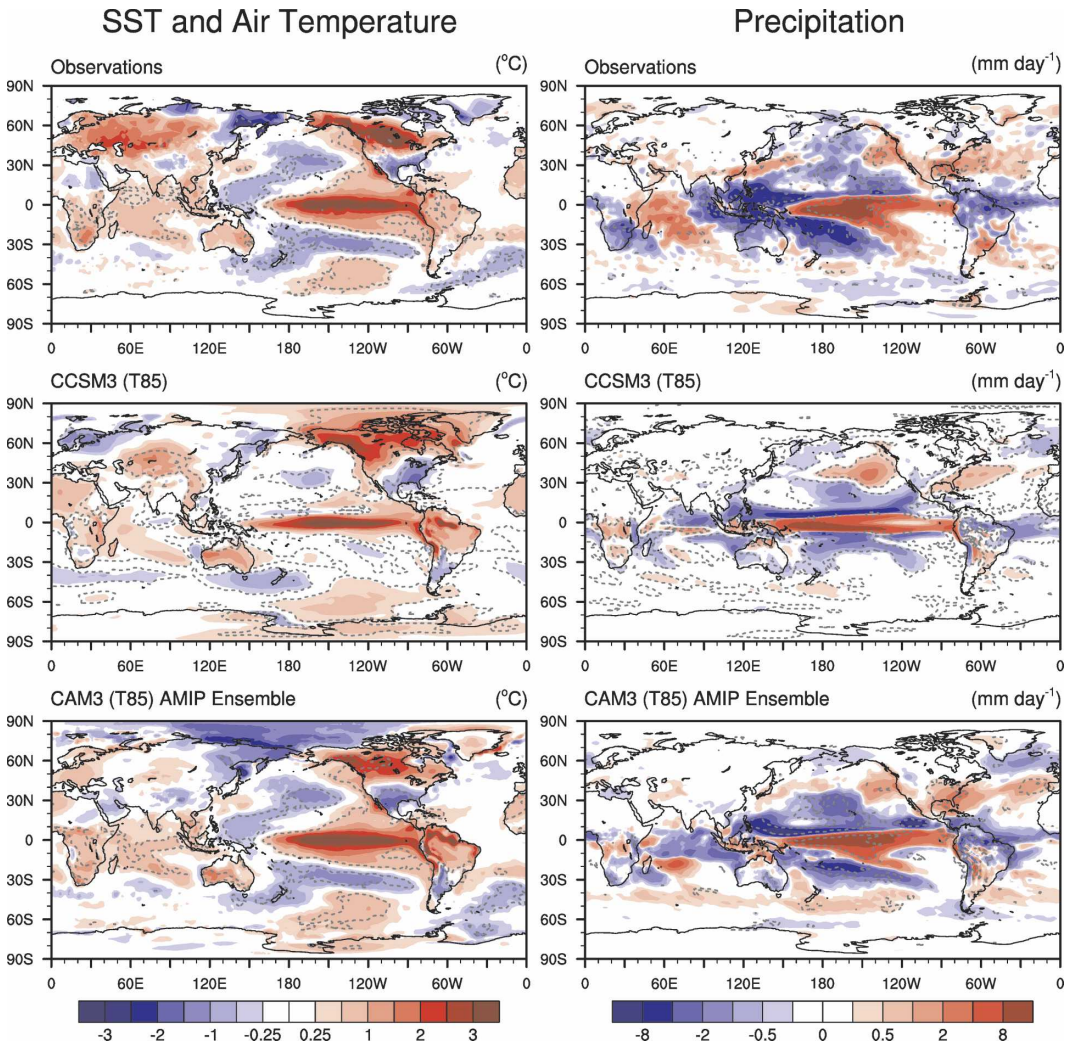

FIG. 6. Warm-minus-cold ENSO event anomaly composites of (left) surface temperature (SST over ocean, surface air temperature over land and sea ice) and (right) precipitation during DJF from (top) observations, (middle) CCSM3 (T85), and (bottom) the ensemble mean of the five CAM3 AMIP integrations (T85). Details of the compositing procedure are given in the text. Dashed contours indicate that the anomalies are significantly different from zero at the 99% confidence level based upon a Student's *t* test. Note that observations are missing over sea ice.

tions, the ENSO-induced precipitation changes over the Pacific may be characterized as equatorward shifts of the ITCZ and SPCZ toward the anomalous warming along the equator. This is also true in CCSM3, but because of the more zonal orientation of the model's SPCZ the ENSO precipitation signal takes on a more zonally symmetric appearance. Another reason for the more meridionally confined precipitation response in CCSM3 compared to observations may be the overly narrow equatorial Pacific SST warming and lack of cooling to the north, south, and west.

To ascertain whether differences in the simulated and observed precipitation ENSO composites are related to differences in the SST anomaly distribution, it is instructive to examine the ensemble mean precipitation response from the five CAM3 AMIP integrations at T85 resolution (Fig. 6, bottom; results from the AMIP integrations at T42 resolution look similar: see Web supplement). The AMIP precipitation composite overcomes some of the unrealistic features seen in CCSM3: in particular, the positive rainfall changes over the Pacific are less equatorially confined (note especially the broader southward extension) and the negative anomalies in the SPCZ are stronger and also extend farther south, although not as far as in observations. In addition, the negative anomalies over the

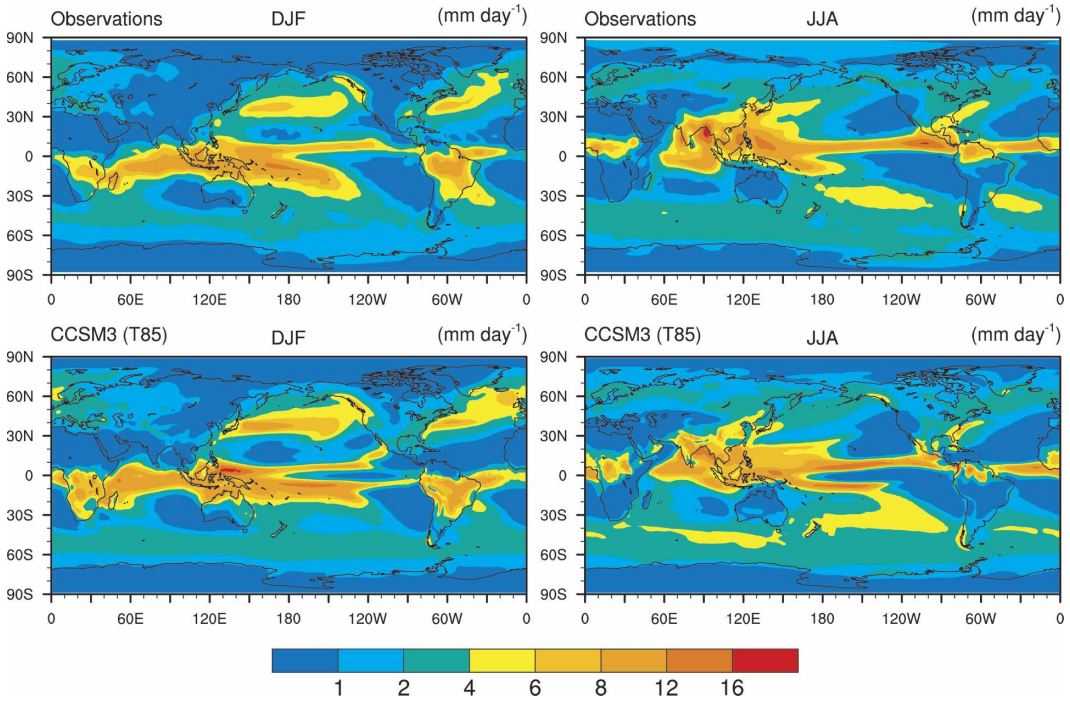

FIG. 7. Climatological precipitation distributions during (left) DJF and (right) JJA from (top) observations and (bottom) CCSM3 (T85). The observed fields are based upon an updated version of the satellite-based estimates of Xie and Arkin (1997) during 1979–2000; the simulated fields are based on model years 400–499.

Indian Ocean are more pronounced, although there are still erroneous positive anomalies over the equatorial portion of the Maritime Continent region. Thus, it appears that the coupled model's tendency for an overly confined equatorial precipitation response to ENSO, with compensating anomalies to the north and south rather than in the zonal direction, is in part a consequence of deficiencies in the model's ENSO SST signal (which could in turn be due to coupled air–sea interactions) rather than an intrinsic property of the atmospheric model itself.

Warm-minus-cold ENSO composite difference maps of surface temperature and precipitation during JJA are shown in Fig. 8. As in DJF, the Pacific SST warming signal in CCSM3 is too narrowly confined about the equator and extends too far to the west, reaching all the way to New Guinea. Also, the model lacks the broad area of cooling in the southwestern Pacific. The precipitation anomalies in CCSM3 exhibit a double-ITCZ-like structure over the Pacific, with reduced precipitation within the climatological locations of the two convergence zones (see Fig. 7) and enhanced precipitation on their equatorward flanks. This is in contrast to the observed precipitation distribution, which exhibits a single dominant ITCZ north of the equator that shifts and expands southward during a warm ENSO event. There is also an equatorward shift of the SPCZ, but this feature is confined to the far western Pacific in JJA, and a reduction of precipitation over the Maritime Continent. Both the model and observations exhibit less rainfall in the Atlantic ITCZ. As in DJF, some of the shortcomings of CCSM3's ENSO precipitation signal in JJA are overcome in the ensemble mean CAM3 AMIP integration (Fig. 8, bottom); however, there are still erroneous positive rainfall anomalies east of the Philippine Islands. The precipitation responses in the T42 versions of CCSM3 and CAM3 AMIP integrations are similar to their T85 counterparts (see the Web supplement).

Warm-minus-cold ENSO composites of SLP during DJF from observations, and CCSM3 and the ensemble-mean CAM3 AMIP integrations at both T42 and T85 resolution, are shown in Fig. 9. The coupled models capture the general features of the observed SLP anomaly field: a tropical dipole between the eastern Pacific and western Pacific/Indian Ocean (e.g., the "Southern Oscillation") and teleconnections to the North and South Pacific. However, CCSM3's simulation of the Southern Oscillation underestimates the amplitude of the positive anomalies over the western Pacific/Maritime Continent and Atlantic, and the maximum negative anomalies over the eastern Pacific are centered along the equator rather than the Southern Hemisphere. In the CAM3 AMIP integration, the am-

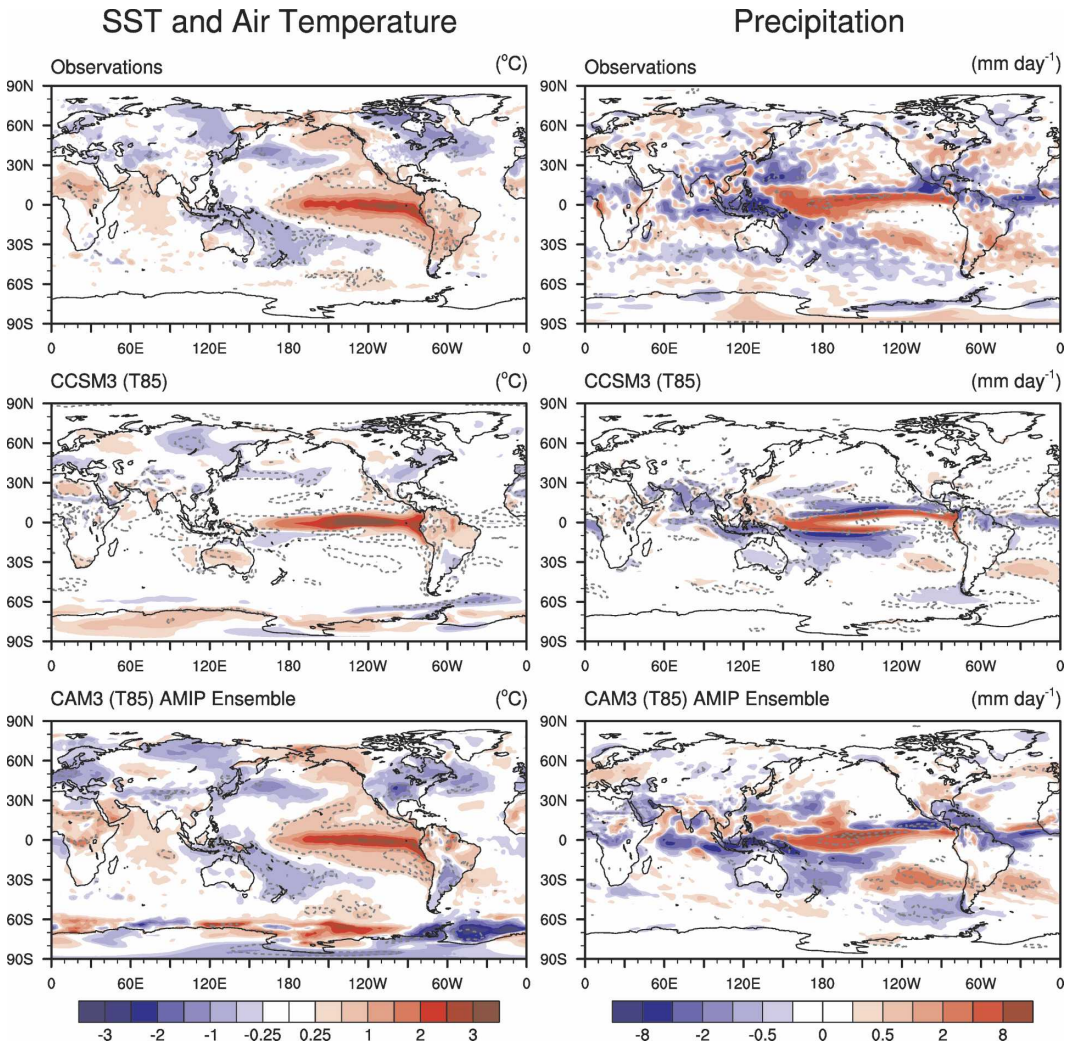

FIG. 8. Same as in Fig. 6, but for JJA.

plitude of the tropical SLP response increases to more realistic levels, particularly in the region of positive anomalies over the western Pacific/Maritime Continent (which also now exhibit a more realistic northeastward tilt into the North Pacific), and the negative anomalies in the eastern Pacific are broader in latitudinal extent more like observations; however, the largest pressure falls are still located on the equator, and the positive anomalies over the tropical Atlantic are still weaker than observed (in the T42 AMIP run, the Southern Oscillation is largely confined to the Pacific/eastern Indian Ocean sector).

CCSM3's simulation of the extratropical SLP response to ENSO is more realistic at T85 resolution than at T42. For example, the negative SLP anomaly center over the North Pacific, corresponding to a deepening of the Aleutian low during warm events, exhibits a realistic amplitude in the T85 model (maximum value of ~9 hPa compared to ~11 hPa in observations) but is too weak in the T42 model only (maximum value of ~4 hPa). Also, the zonal wavenumber-2 aspect of the observed SLP signal over the Southern Ocean, with negative anomaly centers south of New Zealand and South Africa and a positive anomaly center west of the Antarctic Peninsula, is apparent in the T85 model whereas the T42 model exhibits a more zonally symmetric signal.

The magnitude of the Aleutian low SLP response is strengthened in both CAM3 AMIP ensembles relative to CCSM3 at the same resolution, reaching realistic values in the T85 AMIP ensemble (maximum amplitude of ~11 hPa) but remaining weaker than observed in the T42 AMIP ensemble (maximum amplitude of ~7 hPa). The SLP anomaly pattern over northern Eurasia is also improved in the CAM3 AMIP runs compared to the coupled models at both resolutions, where

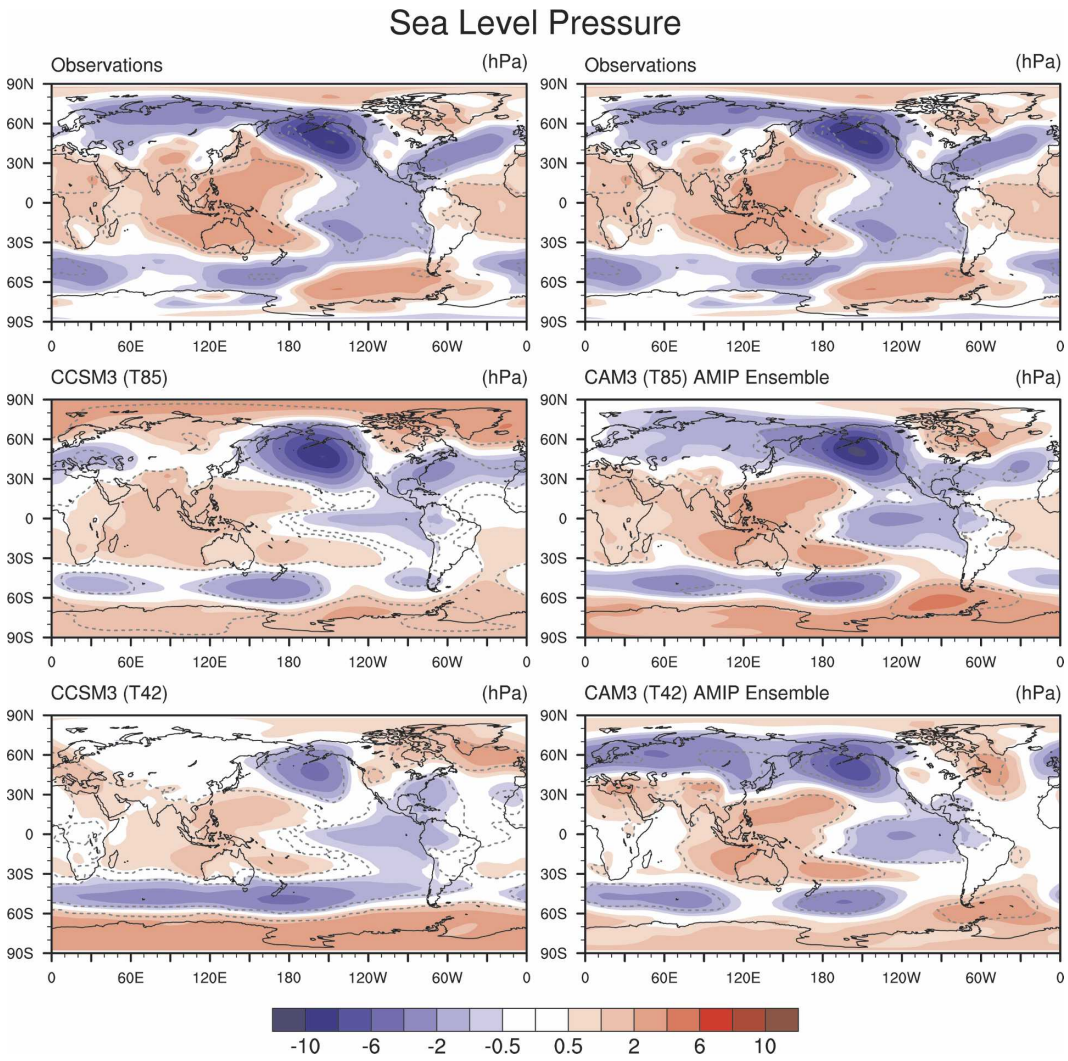

FIG. 9. Warm-minus-cold ENSO event anomaly composites of SLP (hPa) during DJF from (top left and right) observations, CCSM3 at (middle left) T85 and (bottom left) T42 resolutions, and the ensemble mean of the five CAM3 AMIP integrations at (middle right) T85 and (bottom right) T42 resolutions. Details of the compositing procedure are given in the text. Dashed contours indicate that the anomalies are significantly different from zero at the 99% confidence level based upon a Student's *t* test.

the anomalies are now negative as observed. The SLP response over the North Atlantic is improved in the CAM3 AMIP ensemble relative to CCSM3 at T85 resolution but not at T42. Over the Southern Ocean, the centers of the zonal wavenumber-2 pattern in the T85 AMIP ensemble are displaced approximately 30° east of their location in the coupled run at the same resolution (and observations) and their amplitude is too large; a similar zonal wavenumber-2 pattern is present in the T42 AMIP ensemble.

Warm-minus-cold ENSO composites of 500-hPa geopotential heights in DJF are shown in Fig. 10. While the spatial patterns of the geopotential height anomalies are generally well simulated in both versions of CCSM3, the amplitudes are smaller than observed. For example, the band of positive anomalies over the Tropics is weaker by nearly a factor of 2, and the wave train over the North Pacific and North America, which resembles the Pacific–North American (PNA) teleconnection pattern (Wallace and Gutzler 1981), is weaker by a factor of 2 (4) at T85 (T42). The strength of the tropical and extratropical anomalies is improved in the AMIP ensemble compared to CCSM3 at both model resolutions. For example, the magnitude of the tropical response is realistic, and the amplitudes of the three centers of action of the PNA are nearly identical to observations in the T85 AMIP ensemble and ~75% of the observed amplitude in the T42 AMIP ensemble.

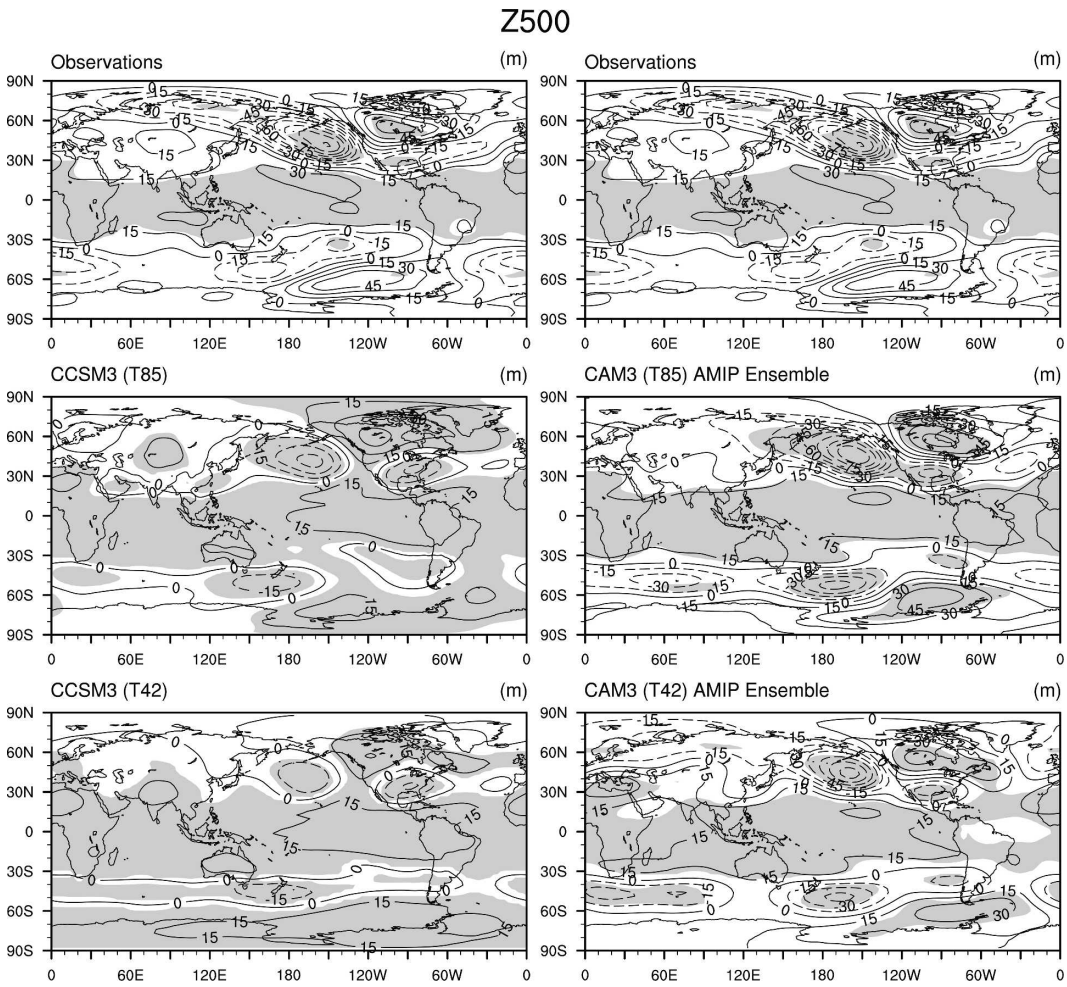

FIG. 10. Same as in Fig. 9, but for geopotential heights at 500 hPa. Positive contours are solid, negative contours are dashed, and the shading indicates where the anomalies are significantly different from zero at the 99% confidence level based upon a Student's *t* test.

The teleconnections to the Southern Hemisphere, which were underestimated in CCSM3, are improved in the AMIP run, although they are generally weaker at T42 than T85.

Warm-minus-cold ENSO composites of SLP in JJA are shown in Fig. 11. In this season, the ENSO SLP signal is located primarily in the Southern Hemisphere (compared to DJF when the signal is global). The positive lobe of the Southern Oscillation is reduced in magnitude compared to DJF in both observations and the models. The negative lobe of the Southern Oscillation in the eastern Pacific in both versions of CCSM3 is split into two centers of comparable strength, one located along the equator directly over the narrow zone of positive SST anomalies and the other in the subtropics. This split is not apparent in either observations or the AMIP integrations, where the amplitude of the SLP anomaly center over the southeast Pacific is more than twice as strong as the equatorial center. The main extratropical feature during JJA is the meridionally oriented dipole over the southeast Pacific, which is captured to some extent by all of the model configurations. There are also weak, but statistically significant, negative SLP anomalies over the North Pacific in observations, a feature that is simulated to some degree by all of the model configurations.

c. Thermocline depth variability in the context of the delayed/recharge oscillator mechanisms

As discussed earlier, a leading dynamical paradigm to explain the ENSO cycle is the delayed oscillator hypothesis, which relies upon oceanic wave processes. In its original formulation (Schopf and Suarez 1988; Suarez and Schopf 1988; Battisti and Hirst 1989) this theory explains deepening of the thermocline in the eastern equatorial Pacific and the growth phase of the

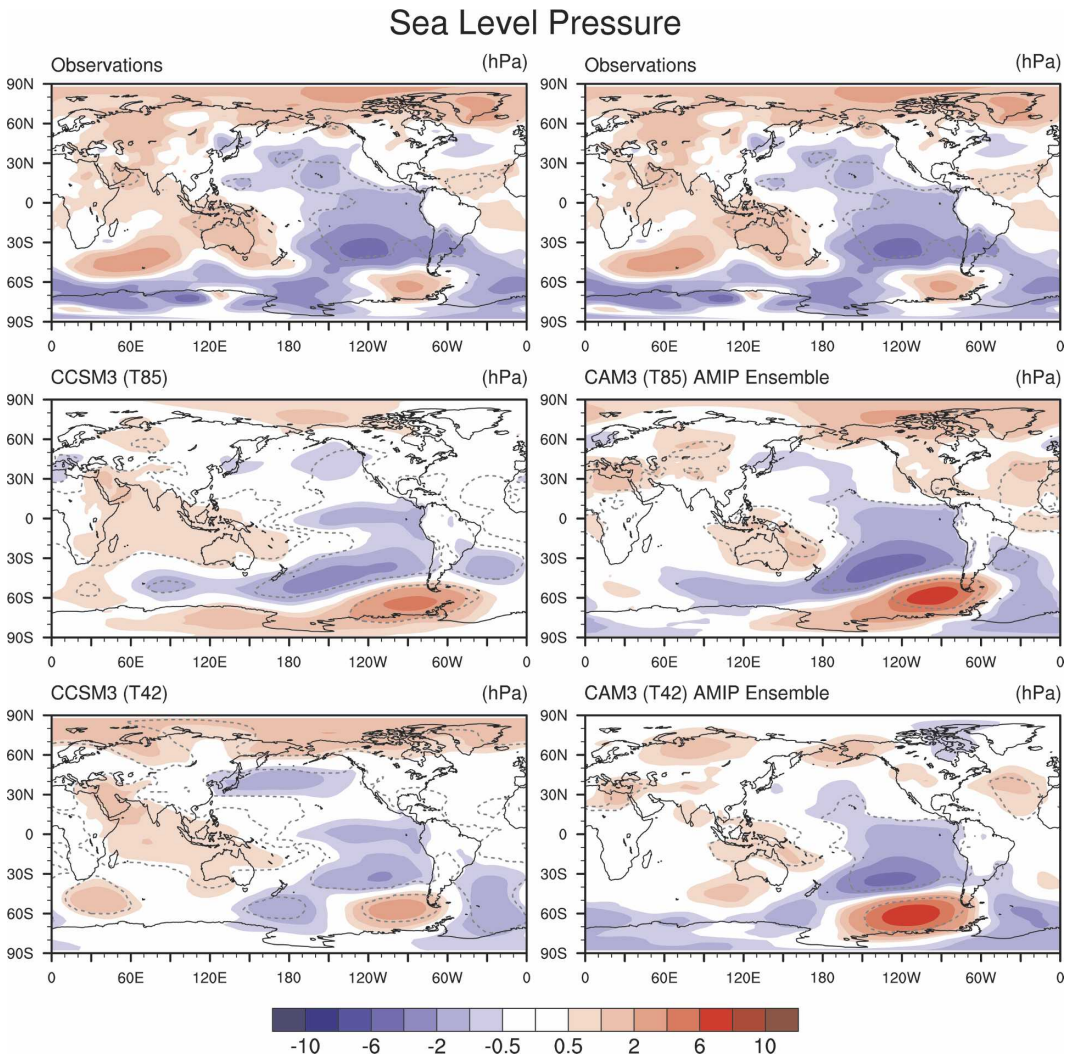

FIG. 11. Same as in Fig. 9, but for JJA.

instability in terms of downwelling equatorial Kelvin waves forced by the anomalous wind stress in the central/western Pacific. The anomalous wind stress also forces first-mode equatorial Rossby waves that propagate westward, reflecting at the western boundary as upwelling Kelvin waves. After reaching the eastern equatorial Pacific, these upwelling waves may reverse the sign of the thermocline depth anomaly, thus acting as the agent responsible for the negative feedback.

The wave processes involved in the delayed oscillator theory can be identified in the evolution of equatorial thermocline depth anomalies in relation to zonal wind stress anomalies from the CCSM3 integration (T85 resolution), as shown in Fig. 12a. For clarity of presentation, we consider monthly anomalies during a 15-yr period (years 430–445 of the model integration). To isolate the ENSO phenomenon, all the data have been bandpass filtered using a Fourier filter with half-power at 1.5 and 5.5 yr (recall that the model ENSO has a dominant time scale of approximately 2–3 yr); however, similar results are obtained without filtering (not shown). From the area of maximum wind stress anomalies (180°–160°W) thermocline depth disturbances appear to propagate eastward, as indicated by the positive slope of the phase lines. Reflection of Rossby waves at the eastern boundary may be responsible for the thermocline depth anomalies east of ~100°W. In some cases (e.g., model years 436, 441.5, 442, and 443), westward-propagating Rossby waves generated around 160°W by the anomalous wind stress can also be detected. Notice that the wind stress anomalies in Fig. 12a are not in equilibrium with the thermocline depth anomalies.

As discussed in previous studies (Schneider et al.

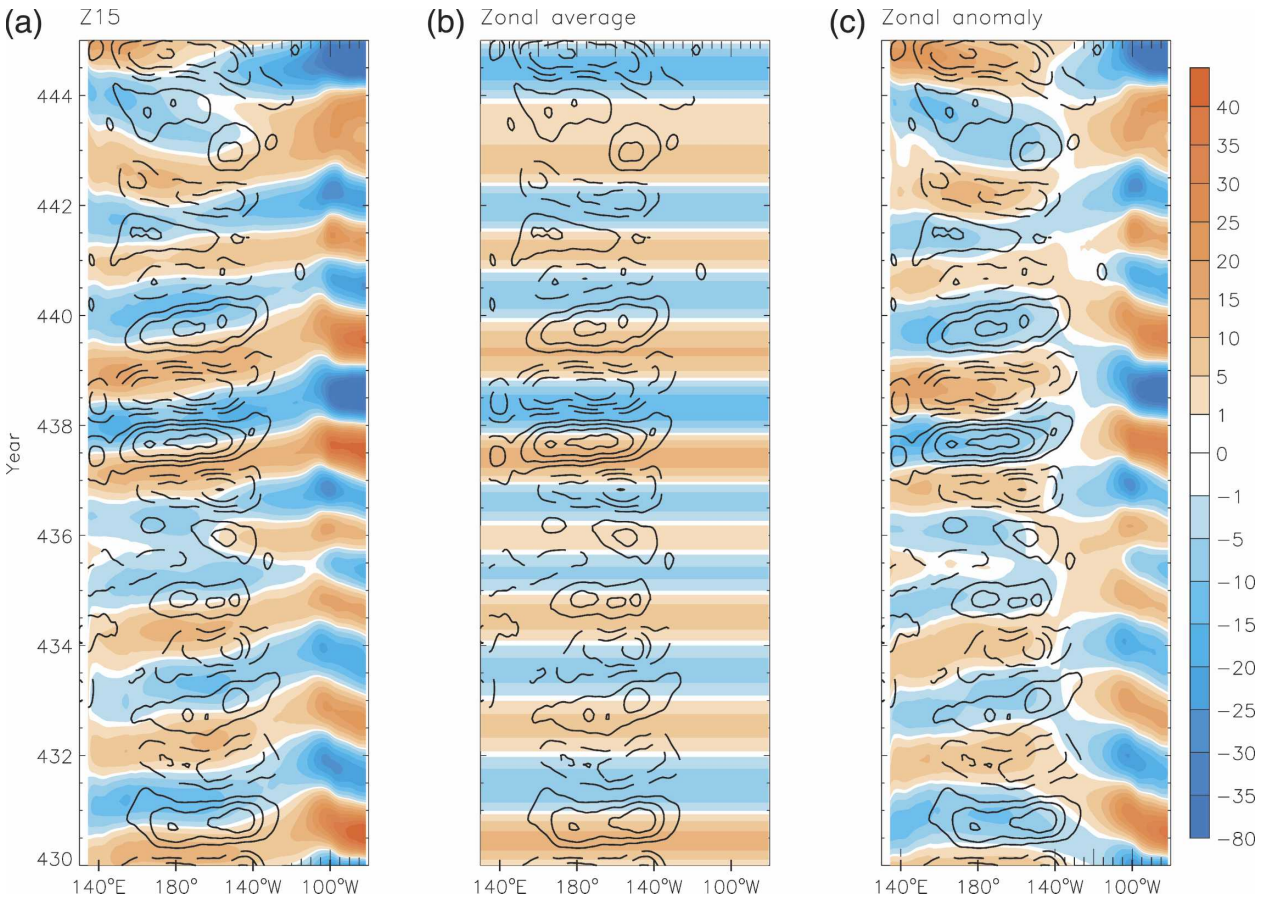

FIG. 12. (a) Evolution of anomalous thermocline depth (given by the depth of the 15°C isotherm; color shading) and zonal wind stress (contours) along the equator during model years 430–445 from CCSM3 at T85 resolution. Positive (negative) values indicate deeper (shallower) thermocline depths relative to the long-term mean seasonal cycle. Solid (dashed) contours indicate positive (negative) wind stress anomalies; the contour interval is 0.05 dyn cm^{-2}. (b), (c) Same as in (a), but for (b) zonally averaged thermocline depth anomalies and (c) thermocline depth anomaly deviations from the zonal mean [the wind stress anomalies remain as in (a)]. All plots are based on monthly anomalies, bandpass filtered using a Fourier filter with half-power at 15 months and 5.5 yr to isolate the ENSO frequency band.

1995; Kirtman 1997) it is useful to decompose the thermocline depth anomalies as $h = \overline{h} + h'$, where $\overline{h}$ is the zonal average of the thermocline depth anomaly, and h' is the deviation from the zonal average. The evolution of $\overline{h}$ is shown in Fig. 12b, and that of h' in Fig. 12c. The zonal anomalies describe changes in the zonal thermocline tilt, and are in phase with the anomalous wind stresses along the equator west of approximately 130°W, with positive wind stress anomalies associated with a flatter thermocline, and vice versa. The nature of the h' signals east of ~120°W and their rapid decay away from the eastern boundary require further investigation. The times of maximum wind stress anomalies generally coincide with the transition phases of $\overline{h}$, so that the two fields are approximately in quadrature. Thus, the zonally averaged thermocline depth anomaly is the quantity that retains the ocean memory, and the disequilibrium between $\overline{h}$ and τ', the anomalous zonal wind stress, is responsible for the system evolution and ENSO phase transition.

In the original formulation of the delayed oscillator framework, the reflection of equatorial Rossby waves at the western boundary is the process responsible for the phase reversal. However, equatorial Rossby waves are too fast to explain the observed ENSO time scale. Extensions of the original delayed oscillator theory (Kirtman 1997 among others) include the effect of Rossby waves forced by extraequatorial wind anomalies. Since the Rossby wave phase speed decreases with increasing latitude, the westward propagation of off-equatorial Rossby waves, and their reflection at the western boundary, will introduce a longer delay and increase the dominant time scale of the cycle. [Other factors such as the sensitivity of the wind stress to SST

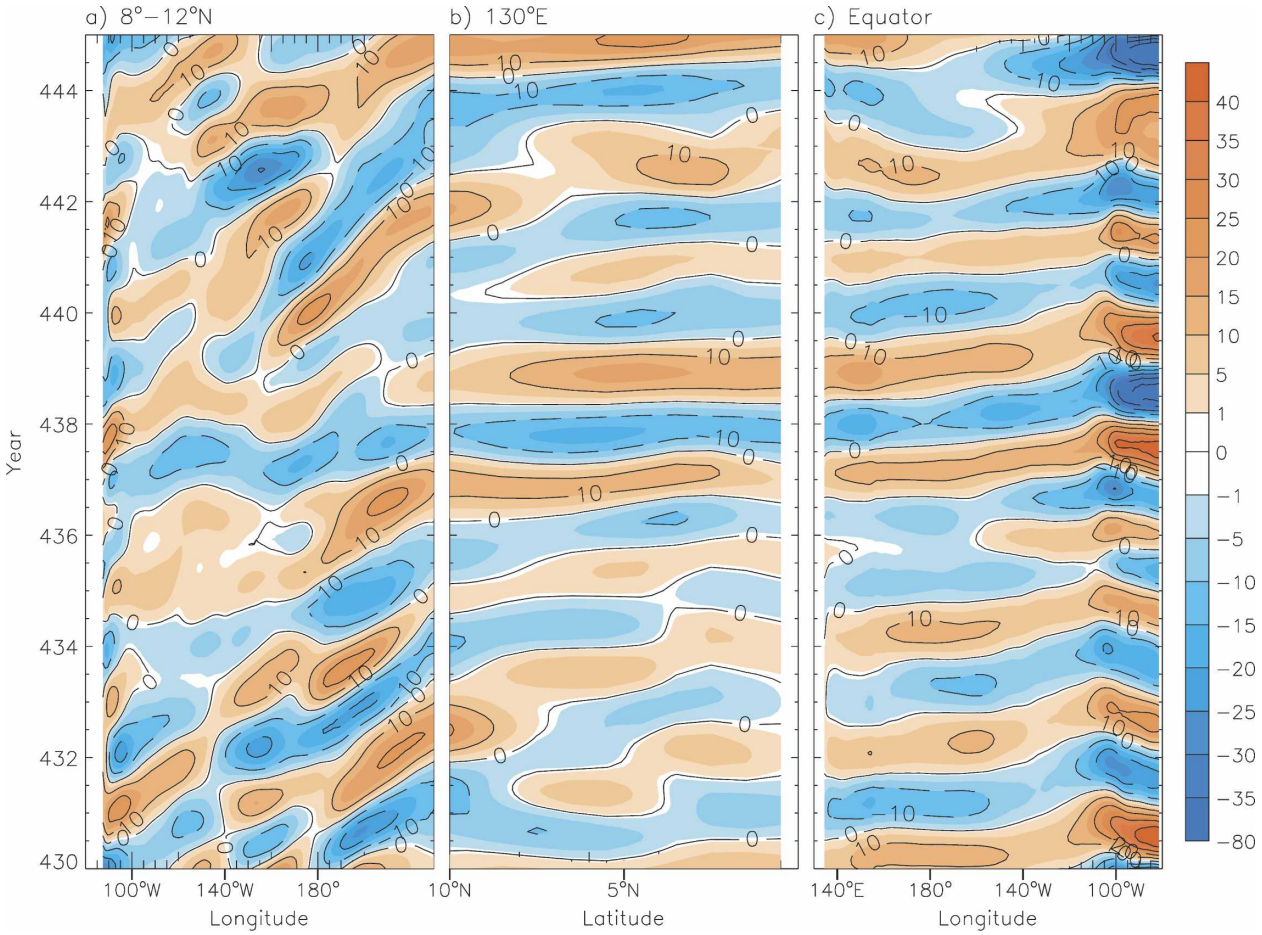

FIG. 13. Evolution of thermocline depth anomalies during model years 430–445 from CCSM3 at T85 resolution along a path from the northern Tropics to the equator. The anomalies averaged (a) over 8°–12°N, plotted from east to west; (b) along the western boundary (~130°W), plotted from north to south; and (c) along the equator, plotted from west to east. Positive (negative) values indicate deeper (shallower) thermocline depths relative to the long-term mean seasonal cycle. All plots are based on monthly anomalies, bandpass filtered using a Fourier filter with half-power at 15 months and 5.5 yr.

anomalies also strongly influence the time scale of the ENSO cycle (Cane et al. 1990; Neelin and Jin 1993).] Evidence of off-equatorial westward-propagating Rossby waves is found in CCSM3 (Fig. 13a). In the 8°–12°N latitude band thermocline depth anomalies originate around 170°W and propagate westward, as indicated by the slope of the phase lines. After reaching the western boundary the waves continue equatorward along the boundary as coastal Kelvin waves (Fig. 13b) and then eastward along the equator as equatorial Kelvin waves (Fig. 13c). Comparison of Fig. 13 and Fig. 12a indicates that some of the equatorial thermocline depth anomalies during model years 430–445 are preceded by thermocline depth anomalies originating around 8°–12°N, 170°W a few years earlier, in agreement with the delayed oscillator theory. Similar results were shown for a modified version of the Climate System Model version 1 (CSM1) by Otto-Bliesner and Brady (2001).

A related conceptual framework to describe the evolution of the zonally averaged equatorial thermocline is the recharge oscillator paradigm (Schneider et al. 1994; Jin 1997a,b). In this theory, which is based on the same physics as the delayed oscillator, the deepening and shoaling of the equatorial thermocline are described in terms of warm-water discharge (recharge) to (from) higher latitudes due to anomalous meridional transport. Instead of focusing on wave propagation as in the delayed oscillator paradigm, the recharge oscillator emphasizes the integrated effect of the waves upon the meridional mass transport. The ENSO cycle within the recharge oscillator paradigm can be schematically summarized as follows: during warm events, the equatorial easterlies are weakened, and the equatorial ther-

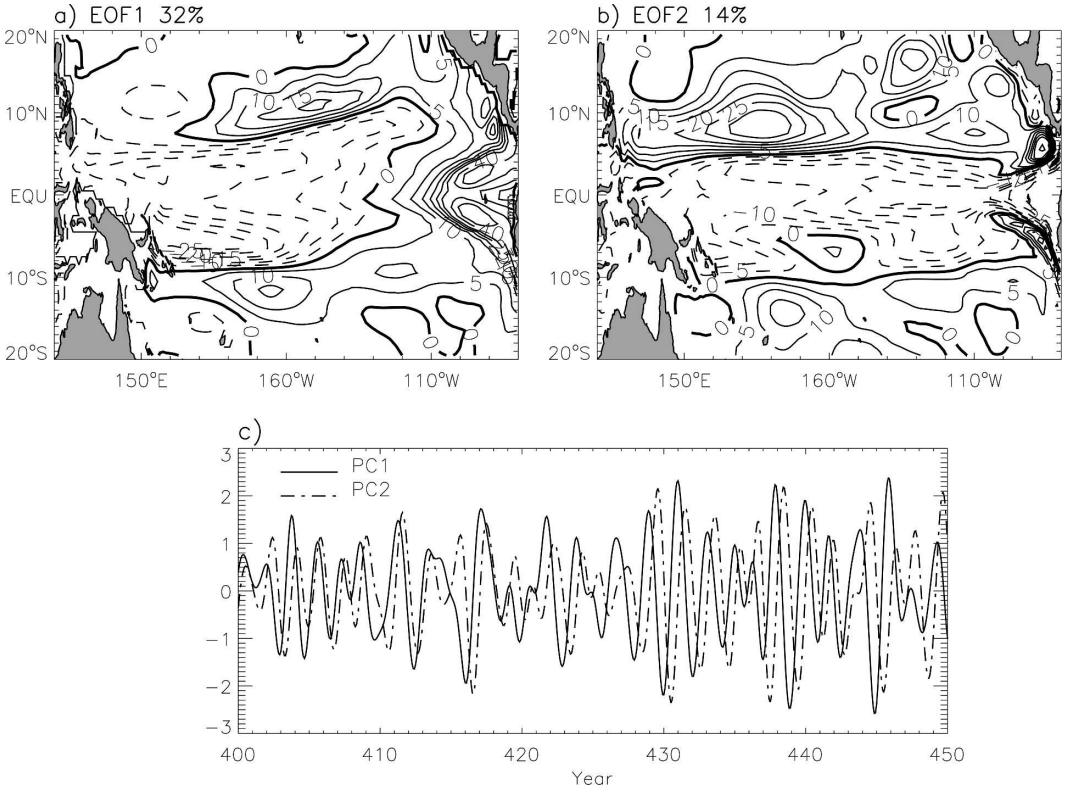

FIG. 14. EOFs (a) 1 and (b) 2 of bandpass-filtered monthly thermocline depth anomalies from CCSM3 based upon model years 400–449, and (c) their associated PC time series. EOFs 1 and 2 account for 32% and 14% of the variance, respectively. The contour interval is 5 m; solid (dashed) contours indicate positive (negative) thermocline depth anomalies. The zero contour is thickened.

mocline is flatter than average. The reduced zonal gradient of thermocline depth is associated with an anomalous poleward Sverdrup transport, which determines a gradual shoaling of the equatorial thermocline and progressively reduces the original SST anomaly in the eastern equatorial Pacific and the associated wind stress anomaly. At this point the thermocline is shallower than average, and equatorial upwelling of colder water will produce a negative SST anomaly in the eastern equatorial Pacific, thus reversing the phase of the oscillation.

To examine the structure of thermocline variations, an EOF analysis is performed on the bandpass-filtered monthly anomalies of thermocline depth (similar results are obtained without filtering; not shown). The leading mode (Fig. 14a), which explains 32% of the variance, is characterized by an east–west dipole pattern, thus capturing variations in the zonal tilt of the thermocline. The second mode (Fig. 14b), accounting for 14% of the variance, has the same sign across the basin with maximum amplitudes in the central and eastern equatorial Pacific, and describes the deepening (shoaling) of the thermocline due to the mass recharge (discharge). The principal components (PCs) of the two modes are highly correlated (Fig. 14c) with a maximum correlation coefficient of 0.8 when EOF1 leads EOF2 by 6 months. Since the dominant time scale is ~2 yr, the two EOFs are approximately in quadrature. Note the similarity between EOF1 and the seasonal thermocline depth anomaly composite in DJF^{+1} (Fig. 5b), and between EOF2 and the composite in JJA^{+1}, 6 months later. PC1 is almost identical to the Niño-3.4 SST index: their correlation coefficient is 0.97 with Niño-3.4 leading PC1 by 2 months (see Fig. 14c). This result is also consistent with the seasonal anomaly composites shown in Fig. 5b.

How realistic are the dominant modes of thermocline variability in CCSM3? As a term of comparison we use thermocline depths from the ocean model forced with observed surface fields during 1958–2000 (the POP simulation). The leading EOFs of the bandpass-filtered thermocline depth anomalies (Fig. 15) have the same general character as those from the coupled simulation (a Fourier filter with half-power at 18 months and 7.5 yr

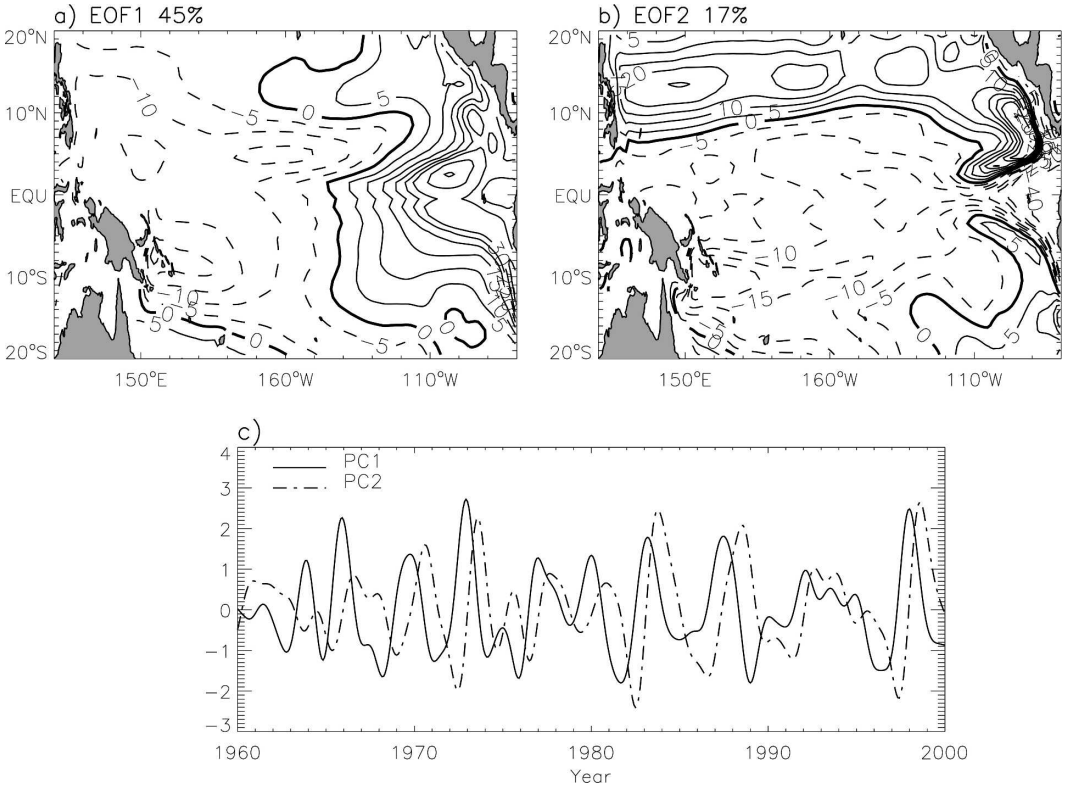

FIG. 15. Same as in Fig. 14, but from the ocean-only simulation forced by observed time-varying surface fields during 1958–2000. To account for the longer ENSO time scales in the ocean-only integration, the bandpass filtering of the monthly thermocline depth anomalies is performed using a Fourier filter with half-power at 1.5 and 7.5 yr.

was used to isolate the ENSO frequency band in the POP simulation due to the longer ENSO period in nature: recall Fig. 3). EOF1 (Fig. 15a) describes variations in the east–west thermocline tilt, while EOF2 (Fig. 15b) is characterized by anomalies of the same sign across the equatorial Pacific and opposite sign north of 7°–10°N. The PCs of the two leading EOF modes are shown in Fig. 15c. The maximum correlation between PC1 and PC2 is 0.8 with PC1 leading PC2 by 9 months. The maximum correlation between PC1 and the Niño-3.4 index is 0.95 with Niño-3.4 leading PC1 by 2 months. Both correlations and phase relationships are similar to those found in CCSM3.

The most striking difference between the EOFs from the coupled model versus those from the ocean-only simulation is the meridional scale of the variability (also evident in the seasonal ENSO anomaly composites shown in Fig. 5). In particular, EOF2 from CCSM3 is bounded by anomalies of opposite sign north of ~5° N and south of ~10°S. whereas in the ocean-only simulation, EOF2 changes sign farther poleward: ~7°–10°N and ~15°–20°S. The ocean-only EOF patterns compare very well in their large-scale characteristics with those computed by Meinen and McPhaden (2000) from (unfiltered) subsurface observations spanning the period 1980–2000.

Why is the meridional scale of the anomalies much narrower in the coupled simulation? The recharge oscillator theory relates the changes of the meridional Sverdrup transport to the thermocline tilt induced by the anomalous zonal wind stress. Thus, the meridional scale of the anomalous zonal wind stress may set the meridional scale of the warm water volume involved in the recharge/discharge process. In Fig. 16 we compare the zonal wind stress from the coupled simulation regressed upon the normalized Niño-3.4 index with the analogous regression field from the ocean hindcast. All time series are bandpass filtered as described above. In the latter case, the zonal wind stress is derived from the NCEP–NCAR reanalyses. Regressions are computed at lag 0, since the maximum zonal wind stress anomalies are quasi-simultaneous with SST variations in the eastern equatorial Pacific. In the coupled case, the positive wind stress anomalies are tightly confined within ~5° of the equator, while in the POP simulation they extend to approximately 7°N and 10°–20°S. Thus, the zonal wind stress anomalies in CCSM3 exhibit a meridional scale that is considerably narrower than observed.

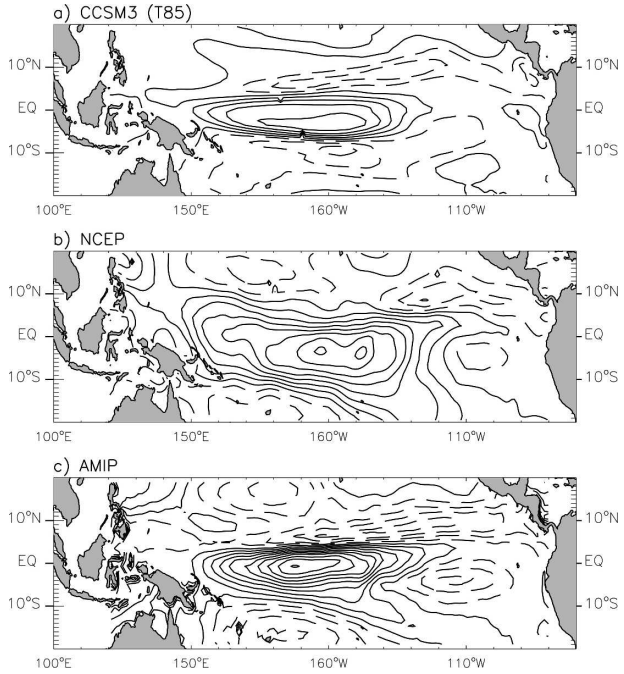

FIG. 16. Regression coefficients of monthly zonal wind stress anomalies upon the normalized monthly Niño-3.4 SST anomaly index, based upon bandpass-filtered data as described in the text, for (a) CCSM3 T85 resolution during model years 350–600, (b) observations (NCEP–NCAR reanalyses during 1958–2000), and (c) the first AMIP integration of CAM3 at T85 resolution forced with observed SSTs during 1950–2000. The contour interval is 0.02 dyn cm^{-2} per standard deviation of the Niño-3.4 index, and solid (dashed) contours indicate positive (negative) wind stress anomalies.

Several studies performed with intermediate coupled models have shown that the period of ENSO is sensitive to the meridional scale of the anomalous zonal wind stress, with a shorter period associated with a narrower meridional scale (Kirtman 1997; An and Wang 2000; Wittenberg 2002; Guilyardi et al. 2003). According to these studies, a broader zonal wind stress anomaly is characterized by a wind stress curl anomaly farther from the equator, which in turn generates off-equatorial Rossby waves with slower velocities and thus longer transit times to the western boundary than a narrower wind stress anomaly. The thermocline signals associated with these extraequatorial Rossby waves tend to reduce the negative feedback of the equatorial Rossby waves, thus promoting ENSO events of longer duration. Alternatively within the framework of the recharge oscillator paradigm, the time scale of recharge/discharge can be expected to increase with increasing warm water volume, which in turn is related to a broader zonal wind stress anomaly. Further mechanistic experiments are needed to test the quantitative relevancy of these ideas for CCSM3.

To address whether the erroneous wind stress structure in CCSM3 is due to deficiencies of the atmospheric model, to coupling between the ocean and atmosphere, or both, we show the regression of zonal wind stress anomalies from the first CAM3 (T85) AMIP simulation upon the observed Niño-3.4 index (Fig. 16c). The positive zonal wind stress regressions from the AMIP run have a slightly broader meridional scale with respect to CCSM3 due to their expansion south of the equator but are still considerably (~60%) narrower than observed. Thus, both inaccuracies of the atmospheric model and coupled feedbacks may be responsible for the unrealistically narrow meridional scale of the zonal wind stress anomalies.

d. The meridional scale of the surface atmospheric response and implications for SST

To gain insight into why the meridional scales of the ENSO zonal wind stress, SST, and thermocline depth anomalies are narrower in CCSM3 compared to observations, we examine in more detail the nature of the SLP and surface heat flux responses. Warm-minus-cold ENSO anomaly composites of annual mean SLP, near-surface wind, and SST are shown in Fig. 17 for two observational datasets (NCEP–NCAR reanalyses and ICOADS), CCSM3 at T85 resolution, and the ensemble mean of the CAM3 AMIP simulations. The annual composites were formed by averaging the four seasonal composites. The reason for comparing NCEP–NCAR with ICOADS is that there are known deficiencies in the NCEP–NCAR reanalysis surface wind and SLP fields over the eastern tropical Pacific because of the complex structure of the atmospheric boundary layer there (Lysne and Deser 2002; Hashizume et al. 2002). Note that ICOADS provides direct measurements of surface winds and SLP from conventional surface-based platforms without any reliance on a data assimilation system.

The CCSM3 fields (Fig. 17, third panel from top) are remarkably symmetric about the equator, with equatorially confined SST and surface wind responses, and maximum negative SLP anomalies, centered directly above the positive SST anomalies. Observational estimates, in contrast, show a stronger degree of equatorial asymmetry, with the largest SLP anomalies (both positive and negative) located south of the equator. [There is some evidence for a relative SLP minimum over the equator in the eastern Pacific in ICOADS, a feature supported by the independently measured southeasterly wind anomalies directly to the south; however, it is weaker than the minimum centered at 25°S, 130°W. The equatorial minimum in observations is hypothesized to result from the direct hydrostatic response of

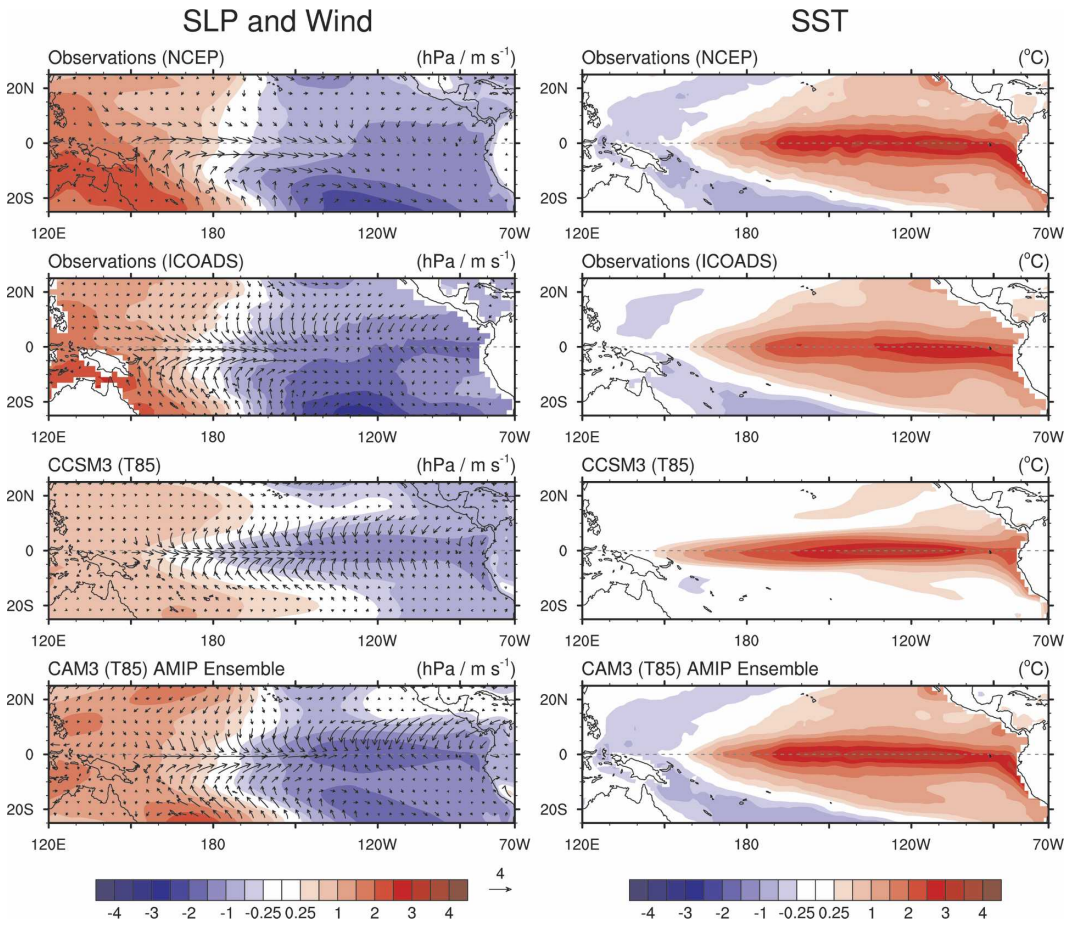

FIG. 17. Warm-minus-cold ENSO anomaly composites of annual mean (left) SLP and surface wind and (right) SST from two different observational datasets (NCEP–NCAR reanalyses during 1950–2000 and ICOADS during 1950–1997), CCSM3 at T85 resolution, and the ensemble mean of the five CAM3 AMIP integrations at T85 resolution. Details of the compositing procedure are given in the text. The scales for all panels are identical (see color bars and reference wind vector at bottom of plot).

the atmospheric boundary layer to underlying SST anomalies (Deser and Wallace 1990; Harrison and Larkin 1996).] The observed SLP anomaly distribution implies that the surface wind response will not be as narrowly confined about the equator as it is in CCSM3. Indeed, southerly wind anomalies extend to at least 20°S over the western half of the basin, a feature that is lacking in the model, and westerly wind anomalies extend to ~10°–20°S as opposed to ~6°S in the model (see also Fig. 16). The SLP and wind responses in the CAM3 AMIP ensemble are more realistic than those in CCSM3, particularly in terms of the increase in amplitude south of the equator. However, the SLP minimum at the equator is still too pronounced relative to that in the Southern Hemisphere, an aspect that may contribute to the narrower meridional scale of the equatorial zonal wind stress anomalies. [It may be noted that the equatorial zonal wind stress response to ENSO in Community Climate Model Version 3 (CCM3), the predecessor to CAM3, was also too meridionally confined (Nigam and Chung 2000).]

Why does CCSM3 yield ENSO SST anomalies that are too equatorially confined compared to nature (see Fig. 17)? One reason may be that deficiencies in the surface wind response lead to errors in the surface energy flux that then affect the SST response. Of course, errors in the ocean model may also contribute to the equatorially confined SST signal, which may in turn force an overly narrow surface wind response that then reinforces the narrow SST anomaly bias via surface flux errors. To explore the notion that surface fluxes may play a role in the pattern of SST anomalies during ENSO, we note that the surface energy flux Q is related to the time tendency of SST according to $d\mathrm{SST}/dt = Q/\rho C_p h$, where ρ and C_p are the density and heat capacity of seawater, respectively, and h is the mixed

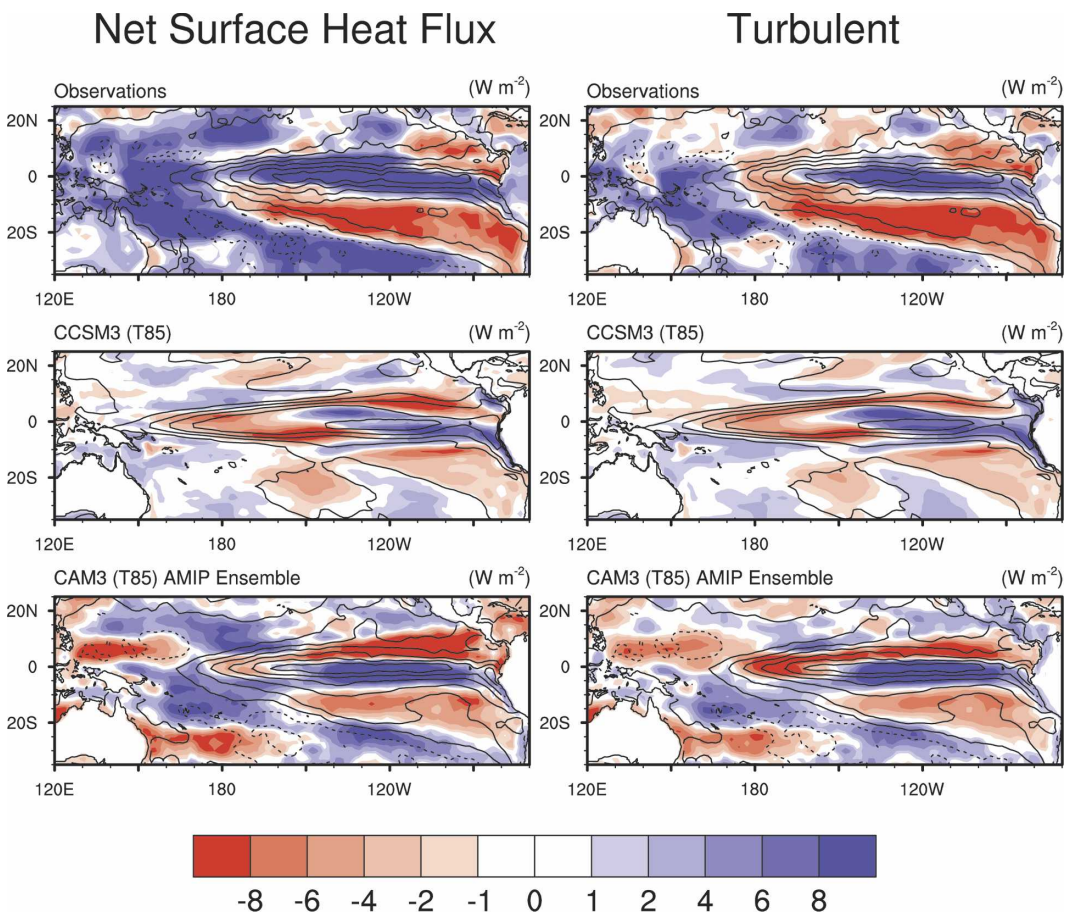

FIG. 18. Regression coefficients of SST anomaly tendencies (contours) and surface heat flux anomalies (net and turbulent component; color shading) upon the normalized Niño-3.4 SST anomaly tendency index from (top) observations, (middle) CCSM3 at T85 resolution, and (bottom) the ensemble mean of the five CAM3 AMIP integrations at T85 resolution. SST tendencies are defined as the difference between SST anomalies in SON minus the previous MAM. Surface fluxes are averages from May through September. The contour interval is 0.25 K per standard deviation of the Niño-3.4 SST tendency index, and the color bar is in units of W m^{-2} per standard deviation of the Niño-3.4 SST tendency index. Surface heat flux regressions are defined as positive downward (e.g., positive values would heat the ocean).

layer depth. To examine the contribution of surface energy flux anomalies to the development of SST anomalies during ENSO events, we examined the change in SST from MAM to SON (denoted SST tendency) in relation to the surface energy flux averaged from May to September (similar results are obtained for averages from March to November and from April to October; not shown). SST tendency and surface flux anomalies were regressed upon the Niño-3.4 SST tendency index for observations, CCSM3 (T85), and the CAM3 AMIP simulations; the results are shown in Fig. 18. The period 1984–2000 was used for the observations because this is the period of record available for the ISCCP radiative fluxes (the turbulent fluxes are from the NCEP–NCAR reanalyses); for compatibility, the same time period was used for the AMIP simulations.

In observations (Fig. 18, top left), upward (negative) surface heat flux anomalies are found over positive SST anomaly tendencies along the equator east of 180° and over the negative SST tendencies in the western Pacific. This indicates that surface heat flux anomalies contribute to forcing the negative SST tendencies, whereas they respond to (and damp) the positive SST tendencies along the equator where oceanic processes such as upwelling and entrainment are expected to play a dominant role. Downward surface heat flux anomalies are found over positive SST tendencies south of the equator (and also a small patch west of Central America), indicating that surface heat fluxes aid in spreading the narrow equatorial SST anomaly tendencies poleward. It is evident that the net surface heat flux regression pattern is dominated by the turbulent flux component

(Fig. 18, top right). The downward turbulent heat flux anomalies that contribute to a southward broadening of the positive SST tendencies in the eastern Pacific are likely due to a weakening of the southeast trade winds associated with the negative SLP anomaly center over the southeast Pacific (Fig. 17).

Like observations, surface heat flux anomalies in CCSM3 generally contribute to forcing the SST anomaly tendency pattern except along the upwelling zone in the eastern Pacific where they act as a damping (Fig. 18, middle). However, because the fluxes are so weak poleward of ~10° latitude in comparison to observations, they result in very small SST anomaly tendencies outside the equatorial band. The relative weakness of the flux anomalies outside the equatorial zone is likely a result of the overly narrow meridional scale of the low-level wind and precipitation responses in the model compared to observations. Like observations, the turbulent flux component dominates the net surface heat flux regression pattern.

The net surface heat flux regressions in the CAM3 AMIP integrations are largely similar to observations, consistent with the generally realistic simulation of the atmospheric circulation response to ENSO SST anomalies (note that both the meridional and zonal components of the wind stress anomalies contribute to the turbulent heat flux anomalies that dominate the net surface heat flux). However, over the far western Pacific along ~30°S and ~5°N, the fluxes would damp (rather than force as observed) the existing negative SST tendencies.

e. ENSO summary

The amplitude and zonal extent of equatorial Pacific SST variations associated with ENSO are well simulated in CCSM3 at both T42 and T85 resolutions and represent an improvement relative to previous generations of the coupled model. In particular, the standard deviation of the monthly Niño-3.4 SST anomaly index is 0.80°C (0.85°C) in CCSM3 T85 (T42), similar to the observed record during the past century (0.75°C). However, the period of ENSO in CCSM3 is shorter than observed (2–2.5 yr compared to 2.5–8 yr), regardless of model resolution (and similar to that in CCSM2). The seasonal evolution of SST anomalies during a composite ENSO cycle exhibits many realistic features, including a tendency for maximum amplitudes in the equatorial Pacific cold tongue near the end of the calendar year, phase transitions during boreal spring, and a delayed SST response over the Indian Ocean. The composite seasonal evolution of thermocline depth anomalies is also in general agreement with observations, with maximum zonal gradients across the equatorial Pacific near the time of peak SST anomalies, and a zonally symmetric distribution indicative of a net discharge (recharge) of equatorial Pacific upper-ocean heat content during the transition from a warm event to a cold one (cold event to a warm one). These characteristics are qualitatively consistent with the delayed oscillator and related recharge oscillator paradigms for ENSO, as are the phase relationships with zonal wind stress anomalies. The main deficiency of CCSM3's ENSO simulation is the excessive equatorial confinement of the atmospheric (precipitation, SLP, and wind stress) and oceanic (SST and thermocline depth) responses relative to observations. This shortcoming is partially overcome in the uncoupled atmosphere and ocean model simulations forced by observed surface boundary conditions, indicating that coupling between the two model components is a contributing cause; however, the atmospheric model itself also appears to play a role. Given the importance of the meridional scale of the surface wind response to the period of ENSO within the simplified framework of the delayed oscillator and recharge oscillator paradigms, this may explain in part the excessively high frequency of ENSO in CCSM3. Further mechanistic experiments are needed to test this idea.

The extratropical SLP response to ENSO in CCSM3 at T85 resolution is generally realistic both in terms of amplitude and spatial pattern, particularly over the North Pacific/North American sector during boreal winter and the South Pacific during boreal summer; the SLP response in CCSM3 at T42 resolution is substantially weaker than observed. For example, the maximum negative SLP anomaly over the Aleutian low pressure center in DJF is –9 hPa (–4 hPa) in CCSM3 T85 (T42) compared to –11 hPa in observations. In agreement with observations, the extratropical atmospheric circulation response to ENSO exhibits an equivalent barotropic structure; however, the amplitude of the response in the midtroposphere is weaker than observed by approximately a factor of 2 (4) at T85 (T42) resolution. Further research is needed to diagnose the mechanisms that lead to the different amplitudes of the atmospheric circulation responses at the two model resolutions.

4. Tropical Atlantic variability

In this section we analyze the performance of CCSM3 in the tropical Atlantic region. Although the TAV does not have the same global impact as variability in the tropical Pacific, it does play an important role in determining climate predictability in the adjoining continental regions, such as the northern Nordeste (NNE) region of Brazil and the Sahel region of Africa

[for a recent review of TAV, see Xie and Carton (2004)]. Coupled GCMs have typically been deficient in their simulation of TAV. Davey et al. (2002), who carried out an intercomparison of the tropical simulation of several coupled GCMs, found that almost all coupled GCMs without flux adjustment have great difficulty in simulating important features of the mean climate of the tropical Atlantic region, such as the east–west gradient of SST at the equator. Simulation of TAV therefore remains an important challenge for coupled climate modeling.

Unlike the tropical Pacific, TAV is not characterized by a single dominant mode of variability like ENSO. This means that we need to examine several different facets of the CCSM3 simulation of the tropical Atlantic region. We will also compare the TAV simulation of CCSM3 to the previous versions of the NCAR coupled model, CCSM2, and CSM1. [For a more detailed assessment of the TAV simulation in CCM3, the atmospheric component of CSM1, see Chang et al. (2000).] The three coupled models, being part of the same family, share some common features. There have also been significant improvements in the physical parameterizations and horizontal resolution in the progression from CSM1 to CCSM3. We would like to examine how these model changes affect the simulations of TAV. We will also consider the role of air–sea coupling, by comparing the coupled CCSM3 simulations to the uncoupled AMIP simulations with CAM3. Since the AMIP simulations use observed SSTs as the surface boundary conditions, any errors in those simulations can usually be attributed to the atmospheric model (with the caveat that AMIP simulations can overestimate surface flux amplitudes). Such attribution is more difficult in the coupled system, because either component could be responsible for the errors. We shall assess the impact of increased horizontal resolution in the atmospheric model by comparing the T42 and T85 AMIP ensemble simulations.

We consider the following major components of TAV: (i) the cross-equatorial SST gradient mode, often simply referred to as the "gradient mode" (e.g., Hastenrath and Heller 1977; Moura and Shukla 1981; Xie and Carton 2004); (ii) the equatorial mode, which is sometimes referred to as the "Atlantic Niño" (Zebiak 1993); and (iii) the remote influence of ENSO (e.g., Covey and Hastenrath 1978; Enfield and Mayer 1997; Saravanan and Chang 2000).

The gradient mode is believed to be an intrinsic mode of variability of the tropical Atlantic region and is characterized by SST anomalies occurring either in the northern or in the southern tropical Atlantic, leading to significant meridional SST gradients near the equator that affect the location of the Atlantic ITCZ (cf. Xie and Carton 2004). This mode has also been referred to as the "Atlantic dipole mode" in the past, but the lack of strong anticorrelation between the northern and southern SST variability suggests that the gradient mode is a more appropriate name. The gradient mode is active primarily during the boreal spring season, when the ITCZ reaches its southernmost location during the annual cycle (Sutton et al. 2000). The driving mechanism for this mode is believed to be local air–sea interaction that is dominated by latent heat flux exchange, rather than wind stress driving (Carton et al. 1996).

The equatorial mode is characterized by SST variability in the eastern equatorial Atlantic and associated variability in the surface wind stress, making it analogous to the ENSO phenomenon in the tropical Pacific (Zebiak 1993). The mode is believed to be driven by the same Bjerknes feedback mechanism as ENSO (Bjerknes 1969), with the surface wind stress and the equatorial upwelling playing an important role. Unlike ENSO, this mode is seen primarily during the boreal summer season (e.g., Sutton et al. 2000).

The remote influence of ENSO is initiated by surface flux anomalies over the tropical Atlantic during the boreal winter, when the ENSO amplitude in the tropical Pacific is at a maximum (e.g., Enfield and Mayer 1997). However, the SST response associated with the remote influence manifests itself during the boreal spring season and is strongest in the Northern Hemisphere. The mechanism for this remote influence is believed to be a combination of the anomalous Walker circulation and other atmospheric teleconnections (cf. Saravanan and Chang 2000).

a. SST

We first consider the mean state of the tropical Atlantic as simulated by CCSM. As the modes of TAV are strongly seasonal, we will consider the climatology of selected seasons, rather than the annual-mean climatology. We focus on the MAM and JJA seasons, when the dominant modes of TAV are most active. Figure 19 shows the simulated JJA mean SST for the three coupled models as compared to observations (HadISST during 1950–2000).

Note that the cold tongue of SST in the eastern equatorial Atlantic is not well simulated by the coupled models. Whereas observations show an equatorial SST of about 25°C near the eastern boundary, the models show SST in excess of 29°C. This model deficiency is most likely associated with errors in the JJA precipitation as simulated by the uncoupled AMIP integrations, where the observed precipitation maximum along the

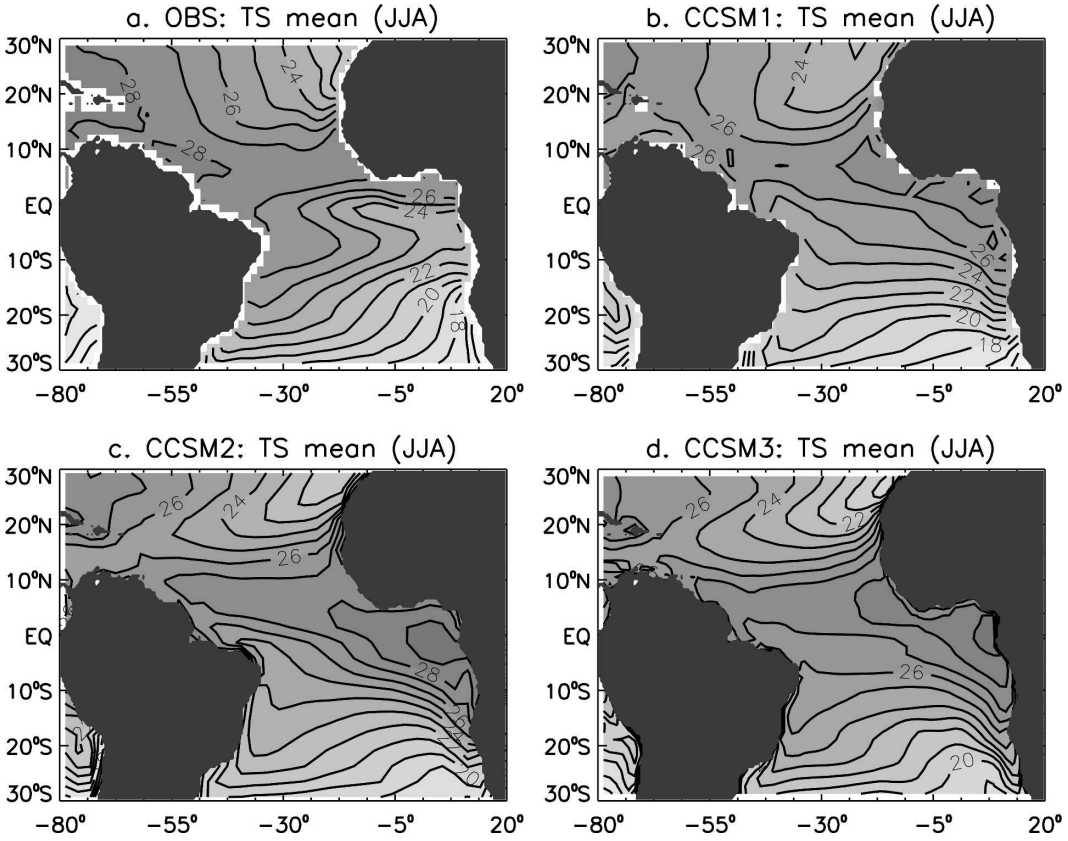

FIG. 19. Climatological mean SST for the JJA season: (a) observations, (b) CSM1, (c) CCSM2, and (d) CCSM3. Contour interval is 1°C.

coast of the Gulf of Guinea occurs too far inland in the simulations (not shown). Such an error would distort coupled air–sea feedbacks associated with the summer monsoon that is believed to be responsible for maintaining the Atlantic cold tongue (Mitchell and Wallace 1992).

The "warm pool" of SST at the western equatorial Atlantic is also not well simulated by the coupled models. In the western region, CCSM3 does perform significantly better with a bias of about –1°C as compared to a bias of −3°C for CCSM1. However, CCSM3 shows a larger cold bias between 20° and 30°N, off the coast of Africa. Overall, it is clear that even the latest generation of the coupled model fails to simulate the sign of the east–west temperature gradient correctly, as was the case with the previous generation of models (Davey et al. 2002). We may expect this error to have a significant impact on the simulation of the equatorial mode of TAV.

We also consider the mean SST for the MAM season, when the gradient mode is most active. Figure 20 compares the observed SST to the simulated SST for CCSM3. In this season, the model performs somewhat better as compared to the JJA season, although there is a significant cold bias in the northern tropical Atlantic. The southern tropical Atlantic simulation of SST compares quite well with observations, except near the coast of Africa. CCSM3 does perform better during the MAM season as compared to CCSM1, which exhibits large cold biases in the northern and equatorial regions (not shown).

Next we consider variability of SST during the MAM and JJA seasons. Figure 21 compares the observed standard deviation of seasonal means to the simulated standard deviations. For the JJA season (Figs. 21a,b), the dominant feature seen in observations is the maximum in SST variability in the central and eastern part of the equatorial Atlantic, coincident with the cold tongue region (Fig. 19a). This corresponds to the equatorial mode of TAV and is essentially absent in the CCSM3 simulation (and also in earlier versions of the coupled model). It seems clear that the simulation of the SST cold tongue needs to be improved to provide a better simulation of the equatorial mode. CCSM3 does simulate the weaker maximum in SST variability seen in the northeastern part of the tropical Atlantic.

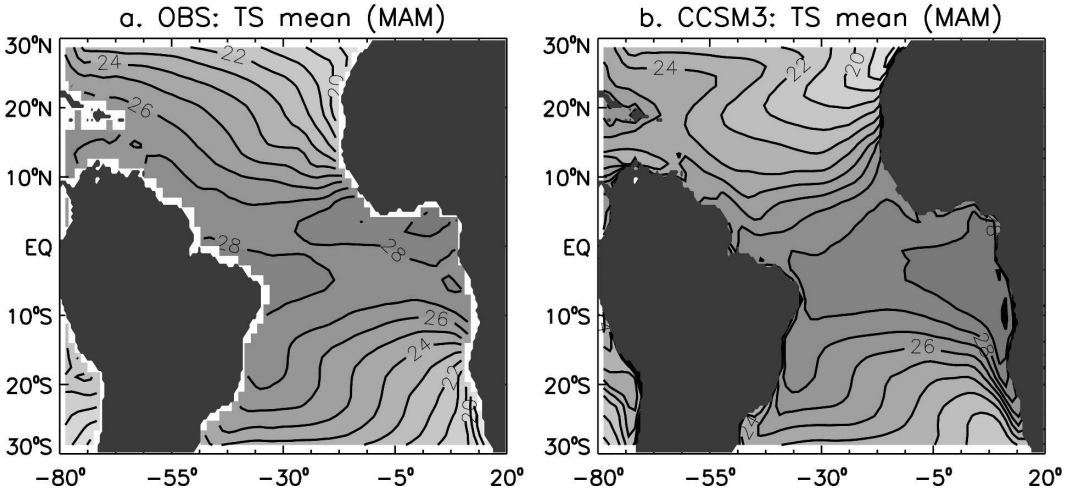

FIG. 20. Climatological mean SST for the MAM season: (a) observations and (b) CCSM3. Contour interval is 1°C.

For the MAM season (Figs. 21c,d), we see the two maxima in variability near the eastern boundary in the two hemispheres, near 10°N and 20°S, with maximum amplitudes of about 1°C. The corresponding maxima in the CCSM3 simulation are somewhat weaker (about 0.7°C) and shifted poleward. Previous versions of the coupled model show very similar features (not shown). This mode of variability corresponds to the gradient of TAV, and we see that the coupled model simulations tend to underestimate it. We also computed EOFs of

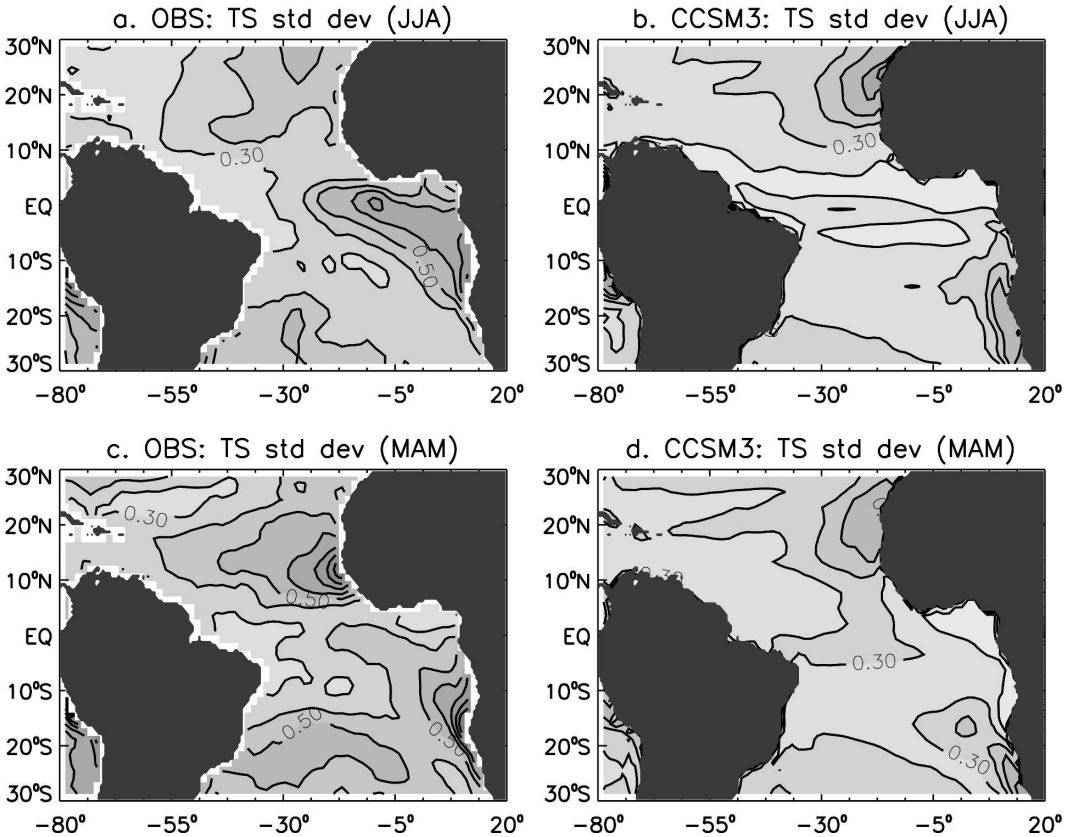

FIG. 21. Climatological standard deviation of seasonal-mean SST: (a) observations for JJA season, (b) CCSM3 for JJA season, (c) observations for MAM season, and (d) CCSM3 for MAM season. Contour interval is 0.1°C.

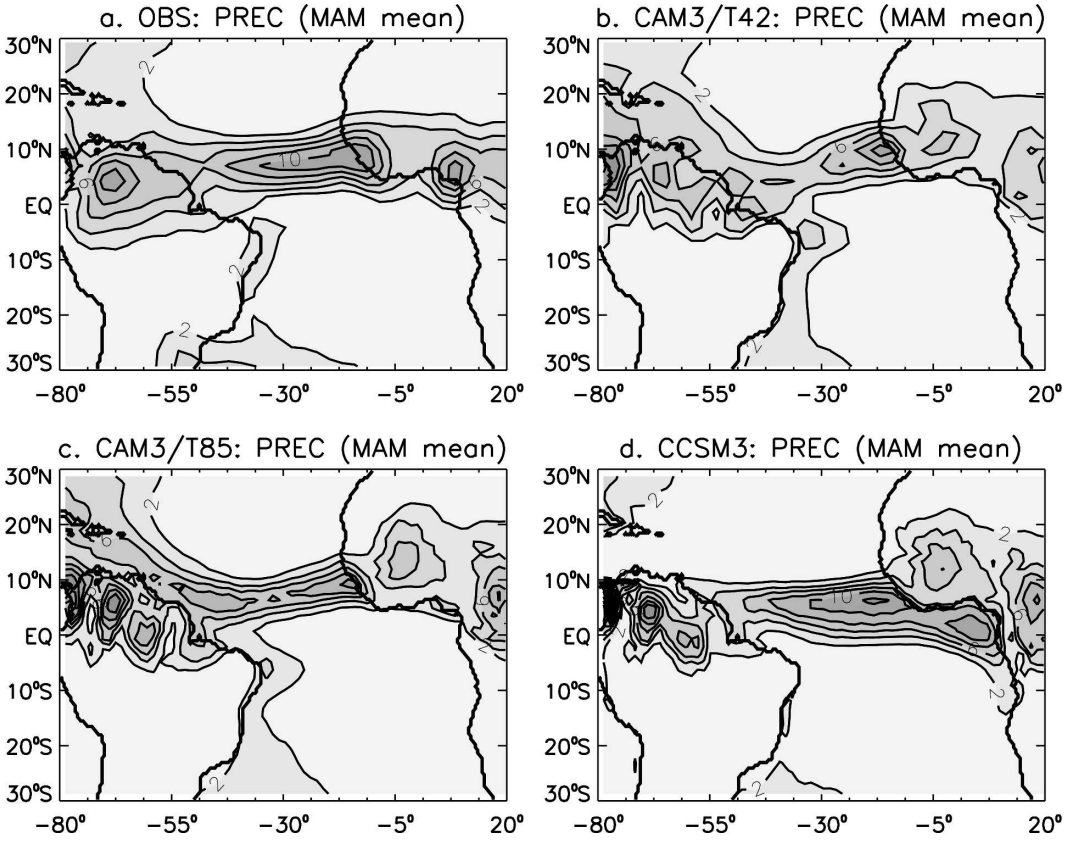

FIG. 22. Climatological mean precipitation for the MAM season: (a) observations, (b) CAM3/T42 AMIP ensemble mean, (c) CAM3/T85 AMIP ensemble mean, and (d) CCSM3 T85 coupled integration. Contour interval is 2 mm day^{-1}.

SST during the MAM season and found that the dominant EOF in all cases displayed the dipolar meridional structure characteristic of the gradient mode (not shown). However, the simulated EOFs had smaller amplitudes, and also failed to capture the northeast–southwest tilt of the boundary between the northern and southern lobes of the dipole seen in the observations.

b. Precipitation

We now consider the mean precipitation simulation of CCSM3 and its atmospheric component, CAM3, during the MAM season. During this season, the interaction between the gradient mode and the location of the ITCZ contributes significantly to TAV. Here we consider the impact of atmospheric model resolution, by comparing the AMIP simulation using the T42 and T85 versions of CAM3. We also consider the role of coupling, by comparing the uncoupled AMIP simulations to the coupled CCSM3 simulation. Figure 22 shows precipitation during the MAM season for observations (1979–2001 period; Xie and Arkin 1997), and three model simulations: CAM3/T42, CAM3/T85, and CCSM3. The main feature over the tropical Atlantic is the ITCZ, which is located near the equator at the western boundary, and north of the equator at the eastern boundary, leading to a northeast–southwest tilt. The uncoupled AMIP simulations overestimate the tilt, with the eastern boundary precipitation maximum occurring too far to the south. There is also the tendency for the ITCZ to split into two zonally oriented parts, at the eastern and western boundaries. Increasing the horizontal resolution from T42 to T85 seems to have little effect on these errors. The coupled CCSM3 simulation also tends to simulate the ITCZ too far to the south, which is consistent with the cold equatorial SST bias near the western boundary seen in Fig. 20b. The coupled model also significantly overestimates the Southern Hemisphere precipitation near the eastern boundary, consistent with the warm SST bias in the region. Overall, we see that the simulated precipitation reproduces the qualitative features seen in observations, such as the tilted ITCZ, but there are significant quantitative errors in the spatial patterns of the precipitation. The precipitation amplitudes in all the simula-

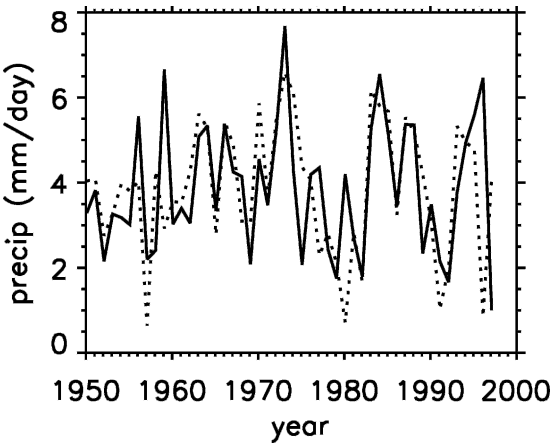

FIG. 23. Area-averaged precipitation over northern Nordeste Brazil (11°–3°S, 46°–38°W) during the MAM season, from 1950 to 1997. The observed values (solid) were obtained from the precipitation dataset of Hulme et al. (1998). The simulated values (dotted) are ensemble averages from the T85 AMIP simulation using CAM3, but renormalized to have the same mean and standard deviation as the observations. (The simulated ensemble-mean precipitation has a mean value about 36% larger than observed, and the standard deviation is about 50% of the observed value.)

tions are roughly consistent with the observed amplitudes.

We know that there is significant predictability of precipitation associated with TAV, especially in the Nordeste region of Brazil during the MAM season (e.g., Chang et al. 2003; Saravanan and Chang 2004). We therefore examine whether the AMIP integrations using CAM3 are skillful in predicting the observed precipitation variability, despite the errors in the simulation of the mean precipitation. Figure 23 shows the observed MAM precipitation in the northern Nordeste (NNE) region (11°–3°S, 46°–38°W) of Brazil for the 2.5° × 3.75° global precipitation dataset of Hulme et al. (1998). Also shown in the figure is the ensemble-mean simulated precipitation from the T85 AMIP integration using CAM3. (The simulated precipitation time series has been renormalized to have the same mean and standard deviation as the observed precipitation time series.) The correlation between the simulated and observed time series is approximately 0.5, indicating that CAM3 is capable of predicting precipitation over NNE Brazil, provided there is prior knowledge of SST variability. It appears that this predictive skill is not very sensitive to model resolution, with the T42 andT85 AMIP integrations showing similar correlation values. However, other models, including previous versions of CAM, show correlation values of 0.6 or greater (e.g., Chang et al. 2003; Giannini et al. 2004). At this time, we do not understand the reasons for this degradation of predictive skill in CAM3.

c. Remote influence of ENSO

Our final diagnostic of TAV will be to consider the remote influence of ENSO on the tropical Atlantic. This remote influence has been the subject of numerous observational and modeling studies (e.g., Enfield and Mayer 1997; Saravanan and Chang 2000), and is sometimes referred to as the tropical atmospheric bridge (e.g., Klein et al. 1999). Figure 24 shows the correlation between MAM SST in the tropical Atlantic and Niño-3 index for the preceding season (DJF). The lagged cor-

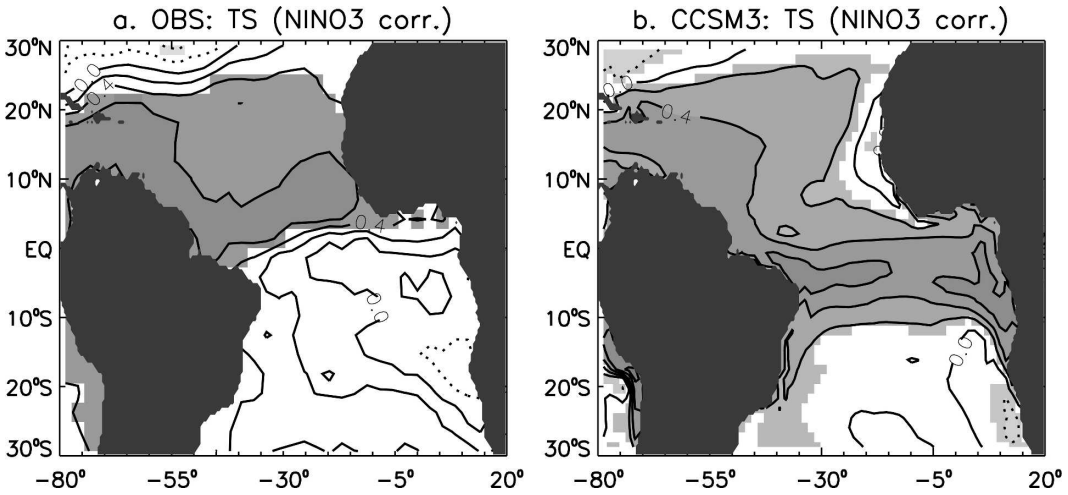

FIG. 24. Correlation between MAM average SST and the Niño-3 index for the preceding DJF season: (a) observations and (b) CCSM3 coupled simulation. Contour interval is 0.2. The shaded regions indicate statistically significant correlations (or regressions) at the 95% level.

relation is appropriate because of the delay in the SST response to the flux anomalies associated with the ENSO signal. The observations show strong (~0.6–0.7) positive correlations over much of the northern tropical Atlantic, but essentially zero correlation right at the equator. The southern tropical Atlantic is characterized by modest (~0.4) negative correlations in the central and eastern parts of the basin. In particular, the band of positive correlations just north of the equator approximately coincides with the mean position of the ITCZ (Fig. 22a).

In CCSM3 simulations, the correlation structure is quite different, with a band of positive correlations along the South American coast in the northern tropical Atlantic, and extending across the basin just south of the equator. Once again, the strongest positive correlations are coincident with the location of the simulated ITCZ (Fig. 22a). The simulated ITCZ is located too far south during the MAM season, and this appears to weaken the ENSO influence just north of the equatorial Atlantic in CCSM3. This suggests that the errors in simulated correlation structure are due to errors in the simulation of the mean precipitation variability. If the simulation of the mean state were to be improved, one might expect the remote influence of ENSO to be properly represented by CCSM3.

d. Summary

CCSM3 shows significant errors in the simulation of TAV. Perhaps the biggest deficiency is the absence of the equatorial "cold tongue" during the boreal summer season. One possible cause of this deficiency could be the poor simulation of the West African monsoon by the uncoupled atmospheric model, which would lead to erroneous simulation of the coupled air–sea feedbacks needed to maintain the cold tongue. Further mechanistic experiments would be needed to confirm this idea. This mean climate error during the boreal summer also has a negative impact on the simulation of the equatorial mode of variability (the "Atlantic Niño"), which is essentially absent in CCSM3.

The simulated mean climate during the boreal spring season shows smaller errors than the summer simulation, although there is a significant cold bias in the northern tropical Atlantic. Correspondingly, the gradient mode of TAV, although underestimated by CCSM3, is somewhat better simulated than the equatorial mode. Given the errors in the mean climate simulation during boreal spring, one would not expect the remote influence of ENSO on tropical Atlantic SST to be simulated very well, and that turns out to be the case.

The simulated mean precipitation has roughly the same amplitude as the observations but exhibits significant errors in the spatial structure tied to errors in the SST simulation. The AMIP integrations exhibit significant potential predictability, with simulated precipitation in the northern Nordeste Brazil region correlating at a value of 0.5 with the observed precipitation. Improved horizontal resolution does not seem to significantly affect the simulated precipitation patterns, or their potential predictability.

Acknowledgments. The model integrations were performed by the National Center for Atmospheric Research (NCAR) and CRIEPI with support and facilities provided by NSF and ESC/JAMSTEC. We thank Dr. Michael Alexander for helpful comments on an earlier draft, and the two anonymous reviewers for their constructive comments and suggestions.

REFERENCES

AchutaRao, K., and K. Sperber, 2002: Simulation of the El Niño Southern Oscillation: Results from the coupled model intercomparison project. *Climate Dyn.,* **19,** 191–209.

Alexander, M. A., I. Blade, M. Newman, J. Lanzante, N.-C. Lau, and J. D. Scott, 2002: The atmospheric bridge: The influence of ENSO teleconnections on air–sea interaction over the global oceans. *J. Climate,* **15,** 2205–2231.

——, and Coauthors, 2006: Extratropical atmosphere–ocean variability in the CCSM3. *J. Climate,* **19,** 2496–2525.

An, S.-I., and B. Wang, 2000: Interdecadal change of the structure of the ENSO mode and its impact on the ENSO frequency. *J. Climate,* **13,** 2044–2055.

Battisti, D. S., and A. C. Hirst, 1989: Interannual variability in a tropical atmosphere–ocean model: Influence of the basic state, ocean geometry and nonlinearity. *J. Atmos. Sci.,* **46,** 1687–1712.

Bjerknes, J., 1969: Atmospheric teleconnections from the equatorial Pacific. *Mon. Wea. Rev.,* **97,** 163–172.

Blanke, B., J. D. Neelin, and D. Gutzler, 1997: Estimating the effect of stochastic wind forcing on ENSO irregularity. *J. Climate,* **10,** 1473–1483.

Boville, B. A., and P. R. Gent, 1998: The NCAR Climate System Model, version one. *J. Climate,* **11,** 1115–1130.

Cane, M., M. Munnich, and S. E. Zebiak, 1990: A study of self-excited oscillations of the tropical ocean–atmosphere system. Part I: Linear analysis. *J. Atmos. Sci.,* **47,** 1562–1577.

Carton, J. A., X. Cao, B. S. Giese, and A. M. da Silva, 1996: Decadal and interannual SST variability in the tropical Atlantic. *J. Phys. Oceanogr.,* **26,** 1165–1175.

Chang, P., R. Saravanan, L. Ji, and G. C. Hegerl, 2000: The effect of local sea surface temperatures on atmospheric circulation over the tropical Atlantic sector. *J. Climate,* **13,** 2195–2205.

——, ——, and ——, 2003: Tropical Atlantic seasonal predictability: The roles of El Niño remote influence and thermodynamic air-sea feedback. *Geophys. Res. Lett.,* **30,** 1501, doi:10.1029/2002GL016119.

Collins, W. D., and Coauthors, 2006: The Community Climate System Model version 3 (CCSM3). *J. Climate,* **19,** 2122–2143.

Covey, D. L., and S. Hastenrath, 1978: The Pacific El Niño phe-

nomenon and the Atlantic circulation. *Mon. Wea. Rev.,* **106,** 1280–1287.

Davey, M., and Coauthors, 2002: STOIC: A study of coupled model climatology and variability in tropical ocean regions. *Climate Dyn.,* **18,** 403–420.

Deser, C., and J. M. Wallace, 1990: Large-scale atmospheric circulation features of warm and cold episodes in the tropical Pacific. *J. Climate,* **3,** 1254–1281.

DeWeaver, E., and S. Nigam, 2004: On the forcing of ENSO teleconnections by anomalous heating and cooling. *J. Climate,* **17,** 3225–3235.

Enfield, D. B., and D. A. Mayer, 1997: Tropical Atlantic sea surface temperature variability and its relation to the El Niño–Southern Oscillation. *J. Geophys. Res.,* **102,** 929–945.

Fedorov, A. V., and S. G. Philander, 2000: Is El Niño changing? *Science,* **288,** 1997–2002.

Giannini, A., R. Saravanan, and P. Chang, 2004: The preconditioning role of tropical Atlantic variability in the development of the ENSO teleconnection: Implications for the prediction of Nordeste rainfall. *Climate Dyn.,* **22,** 839–855.

Glantz, M. H., 2000: *Currents of Change: El Niño and La Niña Impacts on Climate and Society*. Cambridge University Press, 252 pp.

Guilyardi, E., P. Delecluse, S. Gualdi, and A. Navarra, 2003: Mechanisms for ENSO phase change in a coupled GCM. *J. Climate,* **16,** 1141–1158.

——, and Coauthors, 2004: Representing El Niño in coupled ocean–atmosphere GCMs: The dominant role of the atmospheric component. *J. Climate,* **17,** 4623–4629.

Harrison, D. E., and N. K. Larkin, 1996: The COADS sea level pressure signal: A near-global El Niño composite and time series view, 1946–93. *J. Climate,* **9,** 3025–3055.

——, and ——, 1998: El Niño–Southern Oscillation sea surface temperature and wind anomalies. *Rev. Geophys.,* **36,** 353–399.

Hashizume, H., S. P. Xie, M. Fujiwara, M. Watanabe, T. Tanimoto, W. T. Liu, and K. Takeuchi, 2002: Direct observations of atmospheric boundary layer response to SST variations associated with tropical instability waves over the eastern equatorial Pacific. *J. Climate,* **15,** 3379–3393.

Hastenrath, S., and L. Heller, 1977: Dynamics of climatic hazards in northeast Brazil. *Quart. J. Roy. Meteor. Soc.,* **103,** 77–92.

Hoerling, M. P., and A. Kumar, 2002: Atmospheric response patterns associated with tropical forcing. *J. Climate,* **15,** 2184–2203.

Horel, J. D., and J. M. Wallace, 1981: Planetary-scale atmospheric phenomena associated with the Southern Oscillation. *Mon. Wea. Rev.,* **109,** 813–829.

Hulme, M., T. J. Osborn, and T. C. Johns, 1998: Precipitation sensitivity to global warming: Comparison of observations with HadCM2 simulations. *Geophys. Res. Lett.,* **25,** 3379–3382.

Jin, F.-F., 1997a: An equatorial ocean recharge paradigm for ENSO. Part I: Conceptual model. *J. Atmos. Sci.,* **54,** 811–829.

——, 1997b: An equatorial ocean recharge paradigm for ENSO. Part II: A stripped-down coupled model. *J. Atmos. Sci.,* **54,** 830–847.

Kalnay, E., and Coauthors, 1996: The NCEP/NCAR 40-Year Reanalysis Project. *Bull. Amer. Meteor. Soc.,* **77,** 437–471.

Kessler, W. S., 2002: Is ENSO a cycle or a series of events? *Geophys. Res. Lett.,* **29,** 2125, doi:10.1029/2002GL015924.

Kiehl, J., and P. Gent, 2004: The Community Climate System Model, version 2. *J. Climate,* **17,** 3666–3682.

Kiladis, G. N., and H. F. Diaz, 1989: Global climate anomalies associated with extremes in the Southern Oscillation. *J. Climate,* **2,** 1069–1090.

——, and K. C. Mo, 1998: Interannual and intraseasonal variability in the Southern Hemisphere. *Meteorology of the Southern Hemisphere, Meteor. Monogr.,* No. 49, Amer. Meteor. Soc., 307–336.

Kirtman, B. P., 1997: Oceanic Rossby wave dynamics and the ENSO period in a coupled model. *J. Climate,* **10,** 1690–1704.

Kleeman, R., and A. M. Moore, 1997: A theory for the limitation of ENSO predictability due to stochastic atmospheric transients. *J. Atmos. Sci.,* **54,** 753–767.

Klein, S. A., B. J. Soden, and N. C. Lau, 1999: Remote sea surface variations during ENSO: Evidence for a tropical atmospheric bridge. *J. Climate,* **12,** 917–932.

Large, W. G., and G. Danabasoglu, 2006: Attribution and impacts of upper-ocean biases in CCSM3. *J. Climate,* **19,** 2325–2346.

Latif, M., and Coauthors, 2001: ENSIP: The El Niño simulation intercomparison project. *Climate Dyn.,* **18,** 255–276.

Lysne, J., and C. Deser, 2002: Wind-driven thermocline variability in the Pacific: A model–data comparison. *J. Climate,* **15,** 829–845.

McAvaney, B., and Coauthors, 2001: Model evaluations. *Climate Change 2001: The Scientific Basis,* J. T. Houghton et al., Eds., Cambridge University Press, 317–336.

Meinen, C. S., and M. A. McPhaden, 2000: Observations of warm water volume changes in the equatorial Pacific and their relationship to El Niño and La Niña. *J. Climate,* **13,** 3551–3559.

Minobe, S., 1997: A 50–70 yr climatic oscillation over the North Pacific and North America. *Geophys. Res. Lett.,* **24,** 683–686.

Mitchell, T. P., and J. M. Wallace, 1992: On the annual cycle in equatorial convection and sea surface temperature. *J. Climate,* **5,** 1140–1156.

Moura, A., and J. Shukla, 1981: On the dynamics of droughts in northeast Brazil: Observations, theory and numerical experimentation with a general circulation model. *J. Atmos. Sci.,* **38,** 2653–2675.

Neelin, J. D., and F.-F. Jin, 1993: Modes of interannual tropical ocean–atmosphere interaction—A unified view. Part II: Analytical results in the weak-coupling limit. *J. Atmos. Sci.,* **50,** 3504–3522.

Nigam, S., and C. Chung, 2000: ENSO surface winds in CCMS simulation: Diagnosis of errors. *J. Climate,* **13,** 3172–3186.

Otto-Bliesner, B. L., and E. C. Brady, 2001: Tropical Pacific variability in the NCAR Climate System Model. *J. Climate,* **14,** 3587–3607.

Pan, Y. H., and A. H. Oort, 1983: Global climate variations connected with sea surface temperature anomalies in the eastern equatorial Pacific Ocean for the 1958–73 period. *Mon. Wea. Rev.,* **111,** 1244–1258.

Philander, S. G., 1990: *El Niño, La Niña and the Southern Oscillation.* Academic Press, 293 pp.

Rasmusson, E. M., and T. H. Carpenter, 1982: Variation in tropical sea surface temperature and surface wind fields associated with the Southern Oscillation/El Niño. *Mon. Wea. Rev.,* **110,** 354–384.

Rayner, N. A., D. E. Parker, E. B. Horton, C. K. Folland, L. V. Alexander, D. P. Rowell, E. C. Kent, and A. Kaplan, 2003: Global analyses of SST, sea ice, and night marine air temperature since the late nineteenth century. *J. Geophys. Res.,* **108,** 4407, doi:10.1029/2002JD002670.

Ropelewski, C. F., and M. S. Halpert, 1987: Global and regional scale precipitation patterns associated with the El Niño/Southern Oscillation. *Mon. Wea. Rev.,* **115,** 1606–1626.

Saravanan, P., and P. Chang, 2000: Interaction between tropical Atlantic variability and El Niño–Southern Oscillation. *J. Climate,* **13,** 2177–2194.

Saravanan, R., and P. Chang, 2004: Thermodynamic coupling and predictability of tropical sea surface temperature. *Earth Climate: The Ocean-Atmosphere Interaction, Geophys. Monogr.,* Vol. 147, Amer. Geophys. Union, 171–180.

Schneider, E. K., B. Huang, and J. Shukla, 1994*:* Ocean wave dynamics and El Niño. Center for Ocean–Land–Atmosphere Studies Rep. 1, Calverton, MD, 46 pp.

——, ——, and ——, 1995: Ocean wave dynamics and El Niño. *J. Climate,* **8,** 2415–2439.

Schopf, P. F., and M. J. Suarez, 1988: Vacillations in a coupled ocean–atmosphere model. *J. Atmos. Sci.,* **45,** 549–566.

Suarez, M. J., and P. S. Schopf, 1988: A delayed action oscillator for ENSO. *J. Atmos. Sci.,* **45,** 3283–3287.

Sutton, R. T., S. P. Jewson, and D. P. Rowell, 2000: The elements of climate variability in the tropical Atlantic region. *J. Climate,* **13,** 3261–3284.

Trenberth, K. E., 1991: General characteristics of the El Niño Southern Oscillation. *Teleconnections Linking Worldwide Climate Anomalies,* M. Glantz, R. Katz, and N. Nicholls, Eds., Cambridge University Press, 13–42.

——, G. W. Branstator, D. Karoly, A. Kumar, N.-C. Lau, and C. Ropelewski, 1998: Progress during TOGA in understanding and modeling global teleconnections associated with tropical sea surface temperatures. *J. Geophys. Res.,* **103,** 14 291–14 324.

——, J. M. Caron, D. P. Stepaniak, and S. Worley, 2002: Evolution of El Niño–Southern Oscillation and global atmospheric surface temperatures. *J. Geophys. Res.,* **107,** 4065, doi:10.1029/2000JD000298.

Wallace, J. M., and D. S. Gutzler, 1981: Teleconnections in the geopotential height field during Northern Hemisphere winter. *Mon. Wea. Rev.,* **109,** 784–812.

Wittenberg, A. T., 2002: ENSO response to altered climates. Ph.D. thesis, Princeton University, 475 pp.

Woodruff, S. D., R. J. Slutz, R. L. Jenne, and P. M. Steurer, 1987: A comprehensive ocean–atmosphere dataset. *Bull. Amer. Meteor. Soc.,* **68,** 521–527.

Xie, P., and P. A. Arkin, 1997: Global precipitation: A 17-yr monthly analysis based on gauge observations, satellite estimates, and numerical model outputs. *Bull. Amer. Meteor. Soc.,* **78,** 2539–2558.

Xie, S.-P., and J. A. Carton, 2004: Tropical Atlantic variability: Patterns, mechanisms, and impacts. *Earth Climate: The Ocean-Atmosphere Interaction, Geophys. Monogr.,* Vol. 147, Amer. Geophys. Union, 121–142.

Zebiak, S. E., 1993: Air–sea interaction in the equatorial Atlantic region. *J. Climate,* **6,** 1567–1586.

Zhang, Y., W. B. Rossow, A. A. Lacis, V. Oinas, and M. I. Mishchenko, 2004: Calculation of radiative flxues from the surface to top of atmosphere based on ISCCP and other global datasets: Refinements of the radiative transfer model and the input data. *J. Geophys. Res.,* **109,** D19105, doi:10.1029/2003JD004457.